Genetically diverse mouse models of SARS-CoV-2 infection reproduce clinical variation and cytokine responses in COVID-19.

Shelly J. Robertson[1], Olivia Bedard[2], Kristin L. McNally[1], Matthew Lewis[1], Chad Clancy[3], Carl Shaia[3], Rebecca M. Broeckel[1], Abhilash I. Chiramel[4], Gail L. Sturdevant[1], Elvira Forte[2,†], Christoph Preuss[2], Candice N. Baker[2], Jeffrey Harder[2], Catherine Brunton[2], Steven Munger[2], Daniel E. Sturdevant[5], Craig Martens[5], Steven M. Holland[6], Nadia A. Rosenthal[2,7]* and Sonja M. Best[1]*

[1]Laboratory of Virology, Rocky Mountain Laboratories, National Institute of Allergy and Infectious Diseases, NIH; Hamilton MT USA

[2]The Jackson Laboratory; Bar Harbor Maine USA

[3]Rocky Mountain Veterinary Branch, Rocky Mountain Laboratories, National Institute of Allergy and Infectious Diseases, NIH; Hamilton MT USA

[4]Boehringer Ingelheim, Ingelheim, Germany

[5]Research Technologies Branch, Rocky Mountain Laboratories, National Institute of Allergy and Infectious Diseases, NIH; Hamilton MT USA

[6]Division of Intramural Research, National Institute of Allergy and Infectious Diseases, NIH; Bethesda MD USA

[7]National Heart and Lung Institute; Imperial College London

[†]Springer Nature, New York USA

*co-corresponding authors

One Sentence Summary

Genetically diverse mice display a broad spectrum of clinically relevant responses to SARS-CoV-2 infection, reflecting variability in COVID-19 disease.

ABSTRACT

Inflammation in response to severe acute respiratory syndrome coronavirus-2 (SARS-CoV-2) infection drives severity of coronavirus disease 2019 (COVID-19), with effective versus dysregulated responses influenced by host genetics. To understand mechanisms of inflammation, animal models that reflect genetic diversity and clinical outcomes observed in humans are needed. We report a mouse panel comprising the diverse genetic backgrounds of the Collaborative Cross founder strains crossed to K18-hACE2 transgenic mice that confers high susceptibility to SARS-CoV-2. Infection of CC x K18-hACE2 F1 progeny resulted in a spectrum of weight loss, survival, viral replication kinetics, histopathology, and cytokine profiles, some of which were sex-specific. Importantly, survival was associated with early type I interferon (IFN) expression and a phased proinflammatory response distinct from mice with severe disease. Thus, dynamics of inflammatory responses observed in COVID-19 can be modeled in diverse mouse strains that provide a genetically tractable platform for understanding antiviral immunity and evaluating countermeasures.

INTRODUCTION

The COVID-19 pandemic continues to pose a global threat to public health, affecting over 395M people worldwide to date. Patient responses range from asymptomatic or mild symptoms of infection to severe illness with uncontrolled inflammation[1]. In addition, persistent post-COVID health problems can be severe and include a significant risk for future morbidity and mortality[2]. The dramatic variability in disease presentation is dependent on genetic polymorphisms, age, sex and the presence of underlying conditions[3-5], underscoring the need for research models that reflect the diverse biology and pathology of SARS-CoV-2 infection in order to provide optimal platforms for preclinical development of novel therapeutic strategies.

As the first line of host defense, type I interferon (IFN) is essential for control of virus replication, but its functions in COVID-19 are complex and poorly understood, with evidence for roles in both protective and pathogenic host response[6]. It is currently thought that success of IFN in controlling virus replication and orchestrating an effective inflammatory response may relate to the timing of IFN induction relative to peak SARS-CoV-2 replication, the intensity of IFN expression and the kinetics of response resolution [7]. In humans, favorable outcomes of COVID-19

57 have been associated with robust early IFN responses that are subsequently resolved along with other disease
58 signs[8,9]. However, the more severe manifestations of COVID-19, including reduced oxygen saturation levels, higher
59 inflammatory responses and lower anti-viral antibody responses, have been observed in patients with either an early
60 IFN response that fails to resolve and remains elevated for prolonged periods[8], or an IFN response that is
61 substantially delayed relative to peak virus replication[10-13]. The roles of IFN in a pathogenic response may be linked
62 to failure of control of virus replication. However, late or sustained IFN responses may drive pathogenesis through
63 failure to orchestrate an effective adaptive response, exacerbation of inflammatory monocyte responses and
64 inhibition of tissue repair[6,9]. Thus, experimental models are needed that can inform how timing, magnitude and
65 duration of innate immunity relative to virus replication dynamics determines inflammatory responses and
66 pathology.

67 Current mouse models of COVID-19 are important tools in understanding drivers of inflammatory responses and
68 pathology following infection with SARS-CoV-2, but are typically generated on invariant inbred backgrounds,
69 poorly reflecting the diversity of patient outcomes and the impact of host genetics on SARS-CoV-2 infection and
70 response to treatment. Mice humanized for the main cellular receptor for SARS-CoV-2 entry, angiotensin
71 converting enzyme 2[14], are valuable pre-clinical infection models[15]. The most widely used model, K18-hACE2,
72 supports high early virus replication in lung epithelial cells, resulting in inflammatory cell infiltration, interstitial
73 edema and focal consolidation of the lung with rapid lethality[16-21]. However, this model on a standard C57BL/6J
74 genetic background does not reflect the wide variety of COVID-19 outcomes in humans, from asymptomatic to
75 severe[1], that are dependent on genetic polymorphisms, age, sex and the presence of underlying conditions[3-5]. Thus,
76 in the absence of comparative models with different outcomes, it is not known what human response is being
77 modeled by SARS-CoV-2 infection of K18-C57BL/6 mice specifically regarding how IFN response dynamics
78 relates to control of virus replication and pathology.
79

80 Multiple studies have demonstrated the value of using genetically diverse mice to assess the impact of host genetics
81 on infectious disease outcomes [22-26]. Indeed, a single genetic background likely will not capture the range of
82 responses and can fail to model key features of disease[27]. To determine if incorporating genetic diversity could
83 recapitulate the broad phenotypic variation observed in human COVID-19, we crossed the K18-hACE2 strain to the
84 genetically distinct inbred strains A/J, 129S1/SvImJ, NOD/ShiLtJ, NZO/HILtJ, PWK/PhJ, CAST/EiJ, and WSB/EiJ

that along with C57BL/6J comprise the founders of the Collaborative Cross. Together, the CC founder strains represent 90% of the genetic diversity in *M. musculus* populations[28,29], and therefore, can be used to understand genetic regulation of complex immune responses. Notably, NOD/ShiLtJ and NZO/HILtJ mice are commonly used in studies of diabetes and metabolic dysfunction that are factors contributing to COVID-19 severity[30]. In addition to the 8 CC founder strains, BALB/cJ and DBA/2J strains were included because BALB/cJ is widely used in infectious disease modelling, and DBA/2J is a founder strain for BXD strains also used in genetic mapping[31]. Here, we show that by using these genetically diverse mice we can model both early and delayed innate immune responses associated with differing control of virus replication kinetics and pathology in the lung. These mice, therefore, represent invaluable tools to understand how IFN and proinflammatory responses are orchestrated to control SARS-CoV-2 replication and pathology.

RESULTS

Diverse outcomes of SARS-CoV-2 infection in CCxK18-hACE2 F1 mice

F1 progeny of CC founder x K18-hACE2 mice (hereafter abbreviated CC x K18-hACE2) were infected via intranasal inoculation with 10^3 plaque forming units (pfu) SARS-CoV-2 strain nCoV-WA1-2020, MN985325.1 and mice were monitored for 21 days. This virus dose is sub-uniformly lethal in the prototype K18-hACE2 strain (C57BL/6J background), resulting in 80-90% of mice reaching end-point criteria by 7 days post infection (dpi) (Fig.1). Infection was confirmed by seroconversion to SARS-CoV-2 nucleoprotein in all survivors (data not shown). Comparative analysis of the eight CC x K18-hACE2 F1 cohorts documented a broad spectrum of weight loss and survival curves characteristic to each CC founder genotype, some of which were sex-specific (Fig. 1). Highly sensitive strains included C57BL/6J and A/J x K18-hACE2 that lost approximately 20% of their starting weight between 4 and 7 dpi with no clear sex bias. In contrast, CC x K18-hACE2 F1 progeny from PWK, NZO, 129S1/J (Fig. 1), BALB/c and DBA (Fig. S1) were resistant to clinical disease, generally losing 5-10% starting weight with ~80% of mice surviving infection. Finally, CC x K18-hACE2 F1 progeny of three strains (CAST, NOD, WSB) had marked sexual dimorphism in response, with CAST and NOD F1 males susceptible to lethal disease, although differences in weight loss between sexes were not apparent. Yet another phenotype was obtained in SARS-CoV-2 infected WSB F1 progeny, where infection was uniformly lethal in females. Weight loss in WSB F1 males began

113 later than other groups at 6 dpi and surviving males exhibited sustained weight loss until the end of the observation
114 period in contrast to the rapid weight gain associated with recovery of other CC x K18-hACE2 F1 cohorts.
115
116 **Virus replication and dissemination in CCxK18-hACE2 F1 mice**
117 In K18-hACE2 mice, SARS-CoV-2 titers peak in the lung at 2-3 dpi and high titers of virus can be isolated from the
118 central nervous system (CNS) which may contribute to lethality in this model[14,32]. Thus, virus replication kinetics
119 were determined at 3 and 6 dpi in lung and brain of CC x K18-hACE2 F1 cohorts (Fig. 2A, 2B). Sensitive founder
120 strains C57BL/6J and A/J F1 progeny showed high levels of infectious SARS-CoV-2 at 3dpi in lung homogenates
121 that was reduced by 1-2 $\log_{10}$ by 6 dpi with no differences between sexes. At 3 dpi, infectious virus was generally
122 not recovered from the CNS, but ~50% of K18-hACE2 (C57BL/6J) and A/J F1 progeny had high virus burden in
123 the CNS by 6 dpi (10^6-10^8 PFU/g tissue) suggesting a high level of infection disseminated outside of the lung. In
124 contrast, peak lung virus titer in F1 progeny of the most resistant founder strain, PWK, was 150-fold lower than the
125 sensitive strains at 3 dpi and was below the limit of detection at 6 dpi. Control of virus replication in PWK F1s was
126 also evident in the CNS where detection of infectious virus was sporadic. Interestingly, F1 progeny of additional CC
127 founder strains classed as resistant had equivalent peak viral titers in the lung to the sensitive K18-hACE2 and A/J
128 F1 progeny, but they tended to control replication by 6 dpi to levels $1\log_{10}$ lower than sensitive mice and had less
129 virus burden in the CNS. Finally, lung titers in (CAST, NOD and WSB) x K18-hACE2 F1 progeny were not
130 different between males and females despite differences in clinical severity associated with sex. Relative expression
131 of the K18-hACE2 transgene in lung suggested some variability stemming from genetic background, but expression
132 was not associated with clinical phenotypes or peak viral burden (Fig. S2). Thus, F1 progeny of CC x K18-hACE2
133 mouse strains can be further stratified into a) sensitive F1 progeny with high sustained virus replication in lung and
134 CNS (C57BL/6J, A/J), b) resistant F1 progeny associated with lower peak virus titer or earlier control of replication
135 in the lung with no or low dissemination to other organs (PWK, NZO, 129S1/J), and c) F1 progeny with sex bias
136 where resistance is independent of virus titer in the lung suggesting a sex-based difference in host response (CAST,
137 NOD, WSB). Together, these data demonstrate that major differences in the dynamics of SARS-CoV-2 replication
138 and host sensitivity to disease observed in humans can be modeled through use of genetically diverse mouse strains
139 (Summarized in Table 1).
140

141 **Histopathology in lung and brain tissue from SARS-CoV-2 -infected CC x K18-hACE2 F1 progeny**

142 The general pathological changes in SARS-CoV-2-infected K18-hACE2 mice were similar to those previously
143 described [19-21,33] although varied in severity. Inflammatory infiltrates evident by 3 dpi included perivascular
144 lymphocytes with alveolar septa thickened by neutrophils, macrophages and edema. At 6 dpi, pulmonary pathology
145 was multifocal, and consistent with interstitial pneumonia including type II pneumocyte hyperplasia, septal, alveolar
146 and perivascular inflammation comprised of lymphocytes, macrophages and neutrophils, with alveolar fibrin and
147 edema evident. Bronchiolar pathology was not observed in these mice. Lung pathology was classified as none, mild
148 (rare scattered inflammatory foci), moderate (coalescing inflammatory foci) or severe (widespread, large
149 inflammatory foci) as exemplified in Fig. 2C. The classification of 'severe' is a comparative term for these mice, as
150 we generally did not observe pathology in the first 6 days of infection equivalent to that of the more severe Syrian
151 hamster model of COVID-19 [34-36]. Surprisingly, in comparison to F1 progeny of founder strains (K18-hACE2 and
152 A/J) that are highly sensitive to lethal infection, F1 progeny of resistant PWK, female NZO and 129S1/J mice, as
153 well as those of male and female NOD and WSB tended to have higher pathology scores in lungs (Fig. 2D). Lung
154 distribution of viral RNA by RNAscope was limited to type I and II pneumocytes in all strains (Fig. 2B).
155 Importantly, these data suggest that lung pathology can be exacerbated in the context of effective control of SARS-
156 CoV-2 replication but still be associated with rapid recovery. This outcome is modeled by SARS-CoV-2 infection of
157 PWK or NZO F1 progeny. In contrast, higher pathology scores associated with failure to rapidly control virus
158 replication in the lung and higher sensitivity to severe or lethal disease can be modeled by infection of WSB F1
159 progeny.

160

161 In the CNS, pathology was scored as present or absent, as it generally consisted of subtle inflammatory foci,
162 including perivascular cuffing and increased gliosis associated with necrotic cells observed in K18-hACE2 and
163 DBA x K18-hACE2 F1 males (Fig. S3A-C, G). However, pathology in the CNS of CAST x K18-hACE2 F1
164 progeny was striking in that microthrombi were evident in capillaries with extensive hemorrhage in the absence of
165 encephalitis. Although microthrombi were associated with viral RNA distribution in the same area (Fig. S3D-F),
166 microhemorrhage was not observed as extensively in infected K18-C57Bl/6 mice. In addition, infection with 10^3 pfu
167 SARS-CoV-2 was uniformly lethal in male CAST F1 progeny, despite these mice having some of the lowest levels
168 of pathology in the lung at 6 dpi of all mice examined. Thus, CAST mice may be a suitable model for future

169 examination of the host determinants of microthrombus formation sometimes observed in severe human COVID-
170 19[37-39].
171
172 **Impaired cytokine and chemokine response is associated with severe disease**
173 In-depth longitudinal analyses of immune responses in patients with COVID-19 have defined key immunological
174 correlates of disease outcome[7,9,10,40-50]. In addition to high early IFN responses that are subsequently controlled,
175 moderate COVID-19 is associated with increased plasma levels of a core inflammatory signature of pro-
176 inflammatory cytokines, chemokines and growth factors (e.g., IL-1a, IL-1β, IFNα, IL-12p70, and IL-17A) that are
177 effectively resolved during infection[9]. In contrast, severe COVID-19 includes sustained expression of these markers
178 with additional signatures including IL-6, IL-10, IL-18, IL-23, TNF, and eotaxin among others suggesting that
179 specific timing and failure to resolve inflammatory responses are important factors in disease progression[9].
180
181 In SARS-CoV-2-infected CC x K18-hACE2 F1 mice, cytokines and chemokines were quantified in the serum and
182 bronchoalveolar lavage fluid (BAL) at 3 and 6 dpi by multiplex analysis. In general, cytokine levels were much
183 higher in BAL fluid than in serum (Fig. S4A, B; individual data points are provided in Figs. S5-S7). Strikingly in
184 the BAL fluid, IFNα was induced at 3 dpi in all CC x K18-hACE2 F1 mice, but it was highly variable (Fig. 3A). F1
185 mice with C57BL/6J, A/J, CAST and NOD genetic background produced relatively low IFNα compared to PWK,
186 NZO, 129S1/J and WSB that produced 2- to 10-fold higher levels. At 3 dpi, IFNα production was similar in males
187 and females within each strain except for PWK where F1 males produced significantly higher levels than females,
188 and in DBA where F1 females were higher. Importantly, high early IFNα expression at 3 dpi that was resolved by
189 6dpi was associated with survival in resistant ((PWK, NZO and 129S1/J) x K18-hACE2) F1 progeny that most
190 effectively controlled virus replication in the lung and CNS. Thus, PWK F1 progeny represent a model of effective
191 induction and resolution of IFN responses associated with viral control. In comparison, at both 3 and 6 dpi, low
192 levels of IFNα were observed in K18-hACE2 C57Bl/6 mice despite high early virus burden in the lung and failure
193 to effectively control replication by 6dpi (Fig. 3B, C; Fig. S5). The K18-hACE2 C57Bl/6 mice demonstrated
194 considerable virus burden in the CNS by 6dpi suggesting that failure to mount high early IFN responses may be
195 associated with disseminating virus infection. A third important phenotype was observed in WSB F1 progeny that
196 had high IFNα expression in BAL at 3di equivalent to PWK F1 mice, but these mice did not control virus

197 replication in the lung as effectively and had sustained weight loss in surviving individuals. Thus, the WSB strain
198 background may model the situation where high IFN responses are not associated with viral control and may
199 contribute to pathogenesis.
200
201 To further compare the relative expression of immune effectors in BAL fluid, unsupervised hierarchical cluster
202 analysis was performed on data from sensitive (K18-hACE2 and A/J x K18-hACE2) and three resistant strains that
203 did not show a sex bias ((PWK, NZO, 129S1/J) x K18-hACE2). SARS-CoV-2-infected mice grouped into four
204 general clusters each with distinct profiles of cytokine and chemokine expression. As shown in Fig. 3D, Cluster 1
205 was comprised of resistant mice at 3 dpi that expressed proinflammatory cytokine IL-6, TH1 cytokines (IL-12p70,
206 IL-27) and chemokines (CXCL10, Gro-α/KC, CCL2, CCL3, CCL4, CCL5, CCL7 and CXCL2) (designated as
207 Group A). At 6 dpi, some Group A cytokines were resolving (IL-6, IL-27, CCL2 and CXCL10) (Fig. 3E; Table 2)
208 while IL-2, IL-4, IL-5, IL-13, IL-18, IL-1b, GM-CSF, eotaxin, TNF-α, IFN-γ, and IL10 (designated as Group B)
209 were added to the cytokine signature in resistant mice (Fig. 3E, Cluster 2). Interestingly, resistant PWK and NZO x
210 K18-hACE2 mice generally exhibited a unique profile characterized by tempered levels of Group A and Group B
211 along with high production of Gro-α/KC, CCL7, CXCL10, CCL2, eotaxin, and IFNγ, at 6 dpi, a timepoint
212 coincident with the most efficient clearance of virus from the lung (Cluster 4). In contrast, sensitive strains
213 generally failed to produce Group A cytokines at 3 dpi (Cluster 3) and if induced, production of both Group A and
214 Group B mediators occurred at the later timepoint (Fig. 3E, Cluster 2).
215
216 Based on statistical analysis of BAL cytokine levels in resistant versus sensitive F1 progeny, several distinct patterns
217 of expression emerged. At 3 dpi, many of the immune mediators showed higher expression in resistant F1 progeny
218 compared to sensitive F1 progeny and included inflammasome associated cytokines (IL-1beta and IL-18), Th1
219 cytokines (IFNγ and IL-12p70) and several immune cell recruiting chemokines (eotaxin, Gro-α/KC, CCL3, CCL4,
220 CCL7 and CXCL2) (Table 2). Resistant F1 progeny also produced high levels of IL-6, IL-27, CCL2 and CXCL10
221 at 3dpi that were then significantly reduced by 6 dpi compared to moderate and sustained expression in sensitive
222 strains (Table 2; Fig. 3E). In contrast, sensitive F1 progeny produced significantly higher levels of IL-10 (immune
223 suppressive cytokine) and CCL4 (monocyte and neutrophil recruiting chemokine) at 6 dpi compared to resistant
224 F1(Table 2; Fig. 3E).

225

226 Although male and female PWK x K18-hACE2 were equally resistant to SARS-CoV-2 lethal infection, innate
227 immune responses differed between sexes, highlighted by males producing significantly higher levels of IFNα in
228 BAL at 3 dpi compared to females (Fig. 3A). To demonstrate these differences, we chose to compare data from
229 resistant (PWK x K18-hACE2) with sensitive K18-hACE2. At 3 dpi, both male and female PWK x K18-hACE2
230 produced higher levels of cytokines and chemokines compared to K18-hACE2 of the same sex. However, female
231 PWK x K18-hACE2 produced a broader set of immune mediators compared to males despite lower IFNα responses
232 (Table 3). Again, these early responses in male and female PWK x K18-huACE2 were resolved by 6 dpi (Table 3)
233
234 Because IFNα plays a key role in orchestrating antiviral immunity and was identified to be strongly associated with
235 disease outcome in these mouse models, we performed a correlation coefficient analysis to determine the
236 relationship between IFNα and other immune mediators, focusing on F1 progeny from K18-hACE2 (sensitive) and
237 PWK x K18-hACE2 (resistant). In PWK mice, high levels of IFNα at 3 dpi positively correlated with a small subset
238 of cytokines (IFNγ, IL-12p70, IL-6, IL-27 and CCL5) and negatively correlated with IL-10, CXCL10 and CXCL2
239 (Fig. 3F). In K18-hACE2 mice, low IFNα production correlated with low expression of these same immune
240 mediators along with pro-inflammatory TNFα and IL-18, and immune cell recruiting chemokines (eotaxin, CCL3
241 and CCL4). Although IFNα expression was resolved to near basal levels in both sensitive and resistant F1 mice at 6
242 dpi (Fig. 3B and 3C) expression correlations between immune mediators increased in sensitive K18-hACE2, but
243 generally decreased in resistant PWK x K18-hACE2 (Fig. 3G), consistent with high dysregulation in K18-hACE2.
244 Therefore, IFNα expression is highly correlated with a common core of inflammatory mediators (IFNγ, IL-12p70,
245 IL-6, IL-27 and CCL5) in both models, making the PWK x K18-hACE2 and K18-hACE2 comparison particularly
246 powerful in understanding how the magnitude of IFNα influences subsequent inflammation.
247

248 In contract to mice with no clear sex-bias in lethality, IFNα production did not correlate with outcome for F1
249 progeny showing sex-bias (CAST, NOD and WSB) x K18-huACE-2). Both males and females of each strain
250 expressed similar IFNα in BAL at 3 dpi (Fig. 3A). CAST and NOD x K18-huACE2 F1 progeny produced relatively
251 low IFNα and minimal levels of innate immune mediators were detected in CAST x K18-huACE2, and particularly
252 NOD x K18-huACE2 (Fig. S4C), although the later better controlled virus replication in the lung by 6 dpi (Fig. 2A).

253 Interestingly, male and female WSB x K18-huACE2 produced some of the highest IFNα among all genetic
254 backgrounds at 3 dpi (Fig. 3A) along with high levels of Group A and Group B cytokines and chemokines (Fig. S4),
255 which may be consistent with significant weight loss observed in both sexes (Fig. 1C). Male and female WSB x
256 K18-huACE2 also controlled virus replication to a similar degree in lung and had relatively low virus infection
257 detected in brain (Fig. 2A). Despite these similarities, females exhibited more severe clinical disease and surviving
258 males slowly recovered (Fig. 1C). These findings suggest that although type I IFN (IFNα) is a key factor in an
259 effective immune response against SARS-CoV-2, the WSB x K18-huACE2 F1 progeny provide a model where
260 early IFN responses is not the sole determinant of disease outcome in these mouse models.
261
262
263 **DISCUSSION**
264
265 Although the COVID-19 pandemic has spurred unprecedented analyses of human cohorts, the drivers of
266 dysregulated inflammation and how they relate to virus replication kinetics in tissues are not understood. Thus,
267 animal models that recapitulate the complexities of human COVID-19 virus replication dynamics and inflammatory
268 responses are essential to better understand mechanisms of protection and pathogenesis. Here, we report an
269 expanded range of SARS-CoV-2 disease phenotypes using F1 progeny from the eight CC founder mouse strains, as
270 well as BALB/cJ and DBA/2J strains, crossed to K18-hACE-2 transgenic mice. The various genetic backgrounds
271 yielded a spectrum of disease phenotypes including severe (C57BL/6J and A/J), severe with sex-bias (CAST/EiJ,
272 NOD/ShiLtJ and WSB/EiJ), and resistant mice exhibiting relatively high pathology but non-lethal disease
273 (PWK/PhJ, NZO/HILtJ, 129S1/SvImJ, DBA/2J and BALB/cJ). Preliminary assessment of host responses in F1
274 progeny suggests that the variable outcomes of SARS-CoV-2 infection in these mouse models are associated with
275 distinct dynamics of innate immunity. Herein, control of virus replication in the lung and host resistance to disease
276 can be independent from the early peak titer, but it is closely associated with a phased amplification and resolution
277 of proinflammatory mediators. These favorable outcomes of COVID-19 are most clearly modeled by examining
278 SARS-CoV-2 infection of PWK and NZO x K18-hACE2 F1 progeny expressing hACE2. In contrast, infection of
279 C57Bl/6 or A/J x K18-hACE2 F1 progeny represent a model of inefficient IFN expression in the lung, failure of
280 effective host control of virus replication and dysregulation of proinflammatory responses[7,9,49,51-53]. Collectively,
281 the CC x K18-hACE-2 F1 panel of mice represent a genetically diverse population and reflect a broader range of

282 host-viral interactions that influence disease outcomes. Importantly, the mouse panel provides much needed tools to
283 further determine the roles of specific signaling intermediates in orchestrating protective vs pathogenic immunity.
284
285 Host genetics is an important determinant of disease severity caused by SARS-CoV-2[54], but specific host
286 factors that are key in protective versus damaging responses are not well defined. In the CC x K18-hACE2 mice,
287 outcomes of infection were largely independent of early virus replication as both sensitive and resistant strains
288 showed similar virus titers in lung at the early timepoint (with the exception of the PWK). Compared to all genetic
289 backgrounds assessed in this study, C57Bl/6J and A/J mice were the most sensitive to lethal SARS-CoV-2 infection.
290 PWK x K18-hACE2 F1 mice exhibited a resistant, non-lethal disease phenotype and this genetic background was
291 the most effective at controlling virus replication in the lung. PWK belong to the *M. m. musculus* subspecies and are
292 genetically distant from the other CC founder strains that include the wild-derived (WSB) and common inbred
293 laboratory strains (C57Bl/6J, A/J, 129S1, NOD and NZO) of *M. m. domesticus* subspecies, and wild-derived *M. m.*
294 *castaneous* subspecies (CAST)[55,56]. Importantly, PWK mice had generally more severe lung pathology at 6 dpi, a
295 timepoint when infectious virus was undetectable. These findings indicate that the PWK genetic background may be
296 a more ideal model to study innate control of virus replication and mechanisms of tissue repair than the current
297 prototype strain, K18-hACE2-C57Bl/6. Genomic profiling studies have demonstrated that some genetic
298 heterogeneity observed among CC founder strains maps to genes associated with immunity[56,57]. Therefore, defining
299 immune responses unique to PWK and other resistant strains will provide important insight into effective
300 mechanisms of immune-mediated control of virus replication *in vivo*.
301
302 Variability in innate immune responses is one of the key contributors implicated in the heterogeneous
303 disease courses observed in human COVID-19[7,11,58]. However, many questions remain as to the timing, magnitude
304 and duration of innate immunity that confer protective versus pathogenic responses to SARS-CoV-2 infection[6]. In
305 CC x K18-hACE2 F1 progeny, the ability to control virus replication and survive infection was most clearly
306 associated with production of IFNα. The kinetics of IFNα production in BAL fluid was rapid in all F1 progeny,
307 peaking by 3 dpi, however, the magnitude of the response was significantly greater in resistant compared to sensitive
308 strains for both males and females. With high levels of IFNα, resistant strains exhibited a phased cytokine and
309 chemokine response characterized by initial upregulation of IL-6 and chemokines that attract monocytes and

310 neutrophils, followed by production of inflammasome-associated cytokines (IL-1β and IL-18), TNFα and tempered
311 upregulation of anti-inflammatory IL-10. In contrast, the innate response in sensitive strains was dampened and
312 delayed, with minimal early upregulation of cytokines and chemokines in BAL fluid. However, if induced at the
313 later timepoint, the innate response included dysregulated production of a broad set of immune mediators. These
314 data suggest that the magnitude of IFNα directly or indirectly influences the cytokine and chemokine signature with
315 distinct profiles associated with moderate (resistant strains) and severe (sensitive strains) disease. Moreover,
316 identification of a core set of immune mediators in these mouse models that correlate with IFNα expression draw
317 key parallels with immune signatures uncovered in human longitudinal studies[9,43]. Together, these findings are
318 consistent with human studies that suggest phased, controlled recruitment of inflammatory cells[10,11]. IFN responses
319 in patients with severe COVID-19 have been characterized as being sustained at high levels for extended periods,
320 low throughout infection, or delayed relative to peak virus replication. In the mouse models presented here,
321 supporting the
322
323 In severe COVID-19 patients, dysregulated innate responses have recently been linked to defects in viral
324 sensing, IFN signaling and antigen presentation in key innate cells including monocytes, dendritic cells as well as
325 maintenance of plasmacytoid DCs, key producers of type I IFNs[59]. Phenotypic analysis of CC founder strains
326 demonstrated heritable variations in immune cells including T cells, NK cells, dendritic cells and plasmacytoid
327 DCs[57,60]. Thus, further studies of the CC x K18-hACE2 F1 models may uncover correlations between different
328 immune cell frequencies and phenotypes, as well as identify the cellular sources of IFN and how that may influence
329 the signature of IFN-driven responses.
330
331 It is clear from these studies that the CC founder x K18-hACE2 panel of F1 mice represent a valuable
332 experimental tool for the comparative study of host immune responses to SARS-CoV-2. However, the occurrence
333 of encephalitis associated with high neuro-invasion of SARS-CoV-2 in some strains of mice may be a potential
334 confounding factor in closely modeling the disease observed in humans. The hACE-2 transgene is driven by the
335 K18 promotor and its expression has a more ubiquitous distribution than the endogenous Ace-2. The spread of virus
336 to the CNS is the result of high levels of hACE2 expression in the brain[32], not typically observed for endogenous
337 Ace-2. These limitations may be addressed by further modifications of the CC founder mouse models engineered to

338 express hACE2 under more normal physiological conditions as has been achieved with humanization of the mouse
339 Ace2 gene, H353K[61]. In addition, recent reports of limited CNS infection in K18-hACE2 mice infected with SARS-
340 CoV-2 via aerosolized route of inoculation indicating that optimized experimental procedures may further improve
341 the mouse model[62]. Alternatively, many of the strain backgrounds used here (including WSB) demonstrated
342 relatively low levels of neuro-invasion and could be further evaluated as a more useful model of certain COVID-19
343 associated pathology, including the disorder known as long-COVID.
344
345 In summary, the phenotypes in diverse mice support a role for the innate immune system in determining
346 COVID-19 severity[7,11,51-53] and can be used to address key knowledge gaps, including mechanisms of innate
347 immune control of virus replication, defining events needed for a well-orchestrated inflammatory response
348 independent of early viral burden, molecular mechanisms of sex-dependent disease severity, and longer-term
349 implications for tissue repair[63] and lung function. Taken together, these observations demonstrate that use of host
350 genetic variation in mice can model different outcomes of SARS-CoV-2 infection, addressing a major deficiency in
351 the toolkit required to combat COVID-19.
352
353 **MATERIALS AND METHODS**
354
355 **Ethics statement**
356 Animal study protocols were reviewed and approved by the Institutional Animal Care and Use Committee (IACUC)
357 at Rocky Mountain Laboratories (RML), NIAID, NIH in accordance with the recommendations in the Guide for the
358 Care and Use of Laboratory Animals of the NIH. All animal experiments were performed in an animal biosafety
359 level 3 (ABSL3) research facility at RML. Standard operating procedures for work with infectious SARS-CoV-2
360 and protocols for virus inactivation were approved by the Institutional Biosafety Committee (IBC) and performed
361 under BSL3 conditions.
362
363 **Virus preparation**
364 SARS-CoV-2 (USA_WA1/2020) from University of Texas Medical Branch (Vero passage 4) was propagated on
365 Vero cells cultured in DMEM supplemented with 10% fetal bovine serum, 1 mM L-glutamine, 50U/ml penicillin
366 and 50ug/ml streptomycin. Culture supernatants were collected at 72 hpi, aliquoted and stored at -80ºC.

367

368 **Mice and virus infection**

369 CC founder x C57BL/6J -K18-hACE2 F1 were provided by The Jackson Laboratories and include the following:
370 B6.Cg-Tg (K18-ACE2)2PrImn/J), 034860; (A/J x B6.Cg-Tg(K18-ACE2)2Prlmn/J)F1/J, 035940; (PWK/PhJ x
371 B6.Cg-Tg(K18-ACE2)2Prlmn/J)F1/J, 035938; (NZO/HlLtJ x B6.Cg-Tg(K18-ACE2)2Prlmn/J)F1/J, 035936;
372 (129S1/SvImJ x B6.Cg-Tg(K18-ACE2)2Prlmn/J)F1/J, 035934; (CAST/EiJ x B6.Cg-Tg(K18-ACE2)2Prlmn/J)F1/J,
373 035937; (NOD/ShiLtJ x B6.Cg-Tg(K18-ACE2)2Prlmn/J)F1/J, 035935; (WSB/EiJ x B6.Cg-Tg(K18-
374 ACE2)2Prlmn/J)F1/J, 035939; (BALB/cJ x B6.Cg-Tg(K18-ACE2)2Prlmn/J)F1/J, 035941; (DBA/2J x B6.Cg-
375 Tg(K18-ACE2)2Prlmn/J)F1/J 035943. Six- to 12-week-old male and female mice were inoculated by the intranasal
376 route with 10^3 pfu of SARS-CoV-2 in a volume of 50ul PBS (Gibco). Prior to inoculation mice were anesthetized
377 by inhalation of isoflurane. Mice were monitored daily for clinical signs of disease and weight loss.

378

379 **Virus titration**

380 Infectious virus in lung and brain tissue was quantified by plaque assay. Tissues were collected in 0.5ml of DMEM
381 containing 2% FBS, 50U/ml penicillin and 50ug/ml streptomycin and immediately frozen. Tissue samples were
382 weighed, and then homogenized using 5mm steel beads and TissueLyzer II high-speed shaker (Qiagen). Ten-fold
383 serial dilutions of homogenates were prepared in duplicate and used to inoculate Vero cells grown in 48-well tissue
384 culture plates. Following 1 hour incubation at 37ºC, the cells were overlayed with 1.5% carboxymethyl cellulose
385 (CMC) in MEM and incubated at 37ºC for 3-4 days. Cells were then fixed in 10%formalin and plaques were
386 visualized by staining with 1% crystal violet diluted in 10% ethanol.

387

388 **Measurement of SARS-CoV-2-specific IgG**

389 Sera were collected at 21 dpi from mice that survived SARS-CoV-2 infection. SARS-CoV-2 spike protein-specific
390 IgG was measured using SARS-CoV2 spike protein serological IgG ELISA kit (Cell Signaling Technology) per
391 manufacturer's instructions.

392

393 **Multiplex cytokine/chemokine analysis**

394 Sera were collected from SARS-CoV-2-infected mice at 3 and 6 dpi by centrifugation of whole blood in GelZ serum
395 separation tubes (Sarstedt). BAL samples were recovered by insufflation of lungs with 1 ml sterile PBS followed by
396 aspiration to collect ~0.5ml volume of fluid. SARS-CoV-2 in sera and BAL fluid was inactivated by using γ-
397 irradiation (2 MRad) and removed from the BSL3 laboratory. Cytokine concentrations in serum and BAL were
398 measured using a 26-Procartaplex mouse cytokine/chemokine panel (ThermoFisher EPX260-26088-901) combined
399 with a Simplex IFN*a* assay (ThermoFisher EPX01A-26027-901). Samples were run on a Luminex Bio-Plex 200
400 system with BioPlex Manager 6.1.1 software.

401 **Histopathology and *in situ* hybridization**

402 Tissues were fixed in 10% neutral buffered formalin for a minimum of 7 days with 2 changes according to IBC-
403 approved standard operating procedure. Tissues were processed with a Sakura VIP-6 Tissue Tek, on a 12-hour
404 automated schedule, using a graded series of ethanol, xylene, and PureAffin. Embedded tissues were sectioned at 5
405 µm and dried overnight at 42°C prior to staining with hematoxylin and eosin. Chromogenic detection of SARS-
406 CoV-2 viral RNA was performed using the RNAscope VS Universal AP assay (Advanced Cell Diagnostics Inc.) on
407 the Ventana Discovery ULTRA stainer using a SARS-CoV-2 specific probe (Advanced Cell Diagnostics Inc.
408 cat#848569). *In situ* hybridization was performed according to manufacturer's instructions.

409

410 **Quantitative real-time PCR**

411 Total lung RNA was extracted from homogenized lysates using the *mir*Vana miRNA Isolation Kit (Invitrogen cat.
412 AM1560) following the manufacturer's protocol for total RNA isolation. Total RNA samples were quantified using
413 a Nanodrop spectrophotometer (Thermo cat. ND-2000C), and reverse transcribed to cDNA using the SuperScript IV
414 VILO Master Mix with ezDNase enzyme (Invitrogen cat. 11766050) following the manufacturer's instructions.
415 Expression of mouse *Ace2*, mouse *Gapdh*, and human ACE2 were quantified by qPCR using the ViiA7 Real-Time
416 PCR System (Thermo cat. 44535545). TaqMan probes targeting mouse *Gapdh* (Thermo probe ID
417 Mm99999915_g1) and human ACE2 (Thermo probe ID Hs01085333_m1) were used in conjunction with the
418 TaqMan Fast Advanced Master Mix (Thermo cat. 4444556) and the ViiA7 Real-Time PCR System with
419 QuantStudio Software (Thermo cat. 44535545). Samples were run in technical triplicate in 10ul reaction volumes on

420 a 384-well plate, and hACE2 transcript abundance values were normalized to m*Gapdh* in each sample and relative
421 expression was calculated using a common reference lung sample (C57BL/6J male) and the delta delta-Ct method.
422

423 **Statistical analysis**

424 Comparison of survival curves in males versus females for each strain was performed using the log-rank (Mantel-
425 Cox) test. One-way analysis of variance (ANOVA) with Tukey's multiple comparison posttest was used to compare
426 cytokine and chemokine levels of BAL and serum. Differences between groups were considered significant at a P
427 value of <0.05. All statistical analyses were performed with graphPad Prism 8.0 (GraphPad Software) or Qlucore
428 Omics Explorer Version 3.7 (Qlucore AB). Correlation analyses were performed by computing Spearman's
429 coefficients and visualized using ggcorrplot. Correlation tests with $P < 0.001$ were displayed.

430 .

431 **Supplementary Materials**

432 Fig. S1. Survival, weight loss and SARS-CoV-2 replication kinetics in BALB/cxK18-hACE2 or DBAxK18-hACE2
433 F1 progeny

434 Fig. S2. Relative expression of human *ACE2* in the lungs of naive CCxK18-hACE2 F1 progeny

435 Fig. S3. Examples of pathology in the brain of SARS-CoV-2-infected CCxK18-hACE2 F1 progeny

436 Fig. S4. Heatmaps of interferon, cytokine and chemokine expression in the serum compared to the BAL of SARS-
437 CoV-2-infected CCxK18-hACE2 F1 progeny.

438 Fig. S5. Interferon, cytokine and chemokine expression in the bronchoalveolar lavage from SARS-CoV-2-infected
439 sensitive and resistant CCxK18-hACE2 F1 progeny.

440 Fig. S6. Interferon, cytokine and chemokine expression in the serum of SARS-CoV-2-infected sensitive and
441 resistant CCxK18-hACE2 F1 progeny

442 Fig. S7. Interferon, cytokine and chemokine expression in the bronchoalveolar lavage of male versus female SARS-
443 CoV-2-infected CCxK18-hACE2 F1 progeny with sex bias (CAST, NOD and WSB).

444 Table S1. Summary of percent survival, weight loss, virus burden and BAL cytokine profiles in K18-hACE2 x CC
445 Founder F1 progeny.

446 Table S2. Summary of statistical analyses of cytokine and chemokine expression in BAL fluid collected from
447 resistant and sensitive K18-hACE2 x CC Founder F1 progeny.

448 Table S3. Summary of statistical analyses of cytokine and chemokine expression in BAL fluid collected from
449 resistant PWK x K18-hACE2 and sensitive K18-hACE2 mice.

450

451 **References**

452 1 Long, Q. X. *et al.* Clinical and immunological assessment of asymptomatic SARS-CoV-2 infections. *Nat*
453 *Med* **26**, 1200-1204, doi:10.1038/s41591-020-0965-6 (2020).
454 2 Mainous, A. G., Rooks, B. J., Wu, V. & Orlando, F. A. COVID-19 Post-acute Sequelae Among Adults: 12
455 Month Mortality Risk. *Frontiers in Medicine* **8**, doi:10.3389/fmed.2021.778434 (2021).

3 Docherty, A. B. *et al.* Features of 20 133 UK patients in hospital with covid-19 using the ISARIC WHO Clinical Characterisation Protocol: prospective observational cohort study. *BMJ* **369**, m1985, doi:10.1136/bmj.m1985 (2020).
4 Richardson, S. *et al.* Presenting Characteristics, Comorbidities, and Outcomes Among 5700 Patients Hospitalized With COVID-19 in the New York City Area. *JAMA* **323**, 2052-2059, doi:10.1001/jama.2020.6775 (2020).
5 Pairo-Castineira, E. *et al.* Genetic mechanisms of critical illness in COVID-19. *Nature* **591**, 92-98, doi:10.1038/s41586-020-03065-y (2021).
6 Wong, L.-Y. R. & Perlman, S. Immune dysregulation and immunopathology induced by SARS-CoV-2 and related coronaviruses — are we our own worst enemy? *Nature Reviews Immunology* **22**, 47-56, doi:10.1038/s41577-021-00656-2 (2022).
7 Schultze, J. L. & Aschenbrenner, A. C. COVID-19 and the human innate immune system. *Cell* **184**, 1671-1692, doi:10.1016/j.cell.2021.02.029 (2021).
8 Cameron, M. J. *et al.* Interferon-Mediated Immunopathological Events Are Associated with Atypical Innate and Adaptive Immune Responses in Patients with Severe Acute Respiratory Syndrome. *Journal of Virology* **81**, 8692-8706, doi:doi:10.1128/JVI.00527-07 (2007).
9 Lucas, C. *et al.* Longitudinal analyses reveal immunological misfiring in severe COVID-19. *Nature* **584**, 463-469, doi:10.1038/s41586-020-2588-y (2020).
10 Bastard, P. *et al.* Autoantibodies against type I IFNs in patients with life-threatening COVID-19. *Science* **370**, doi:10.1126/science.abd4585 (2020).
11 Zhang, Q. *et al.* Inborn errors of type I IFN immunity in patients with life-threatening COVID-19. *Science* **370**, doi:10.1126/science.abd4570 (2020).
12 Galani, I. E. *et al.* Untuned antiviral immunity in COVID-19 revealed by temporal type I/III interferon patterns and flu comparison. *Nat Immunol* **22**, 32-40, doi:10.1038/s41590-020-00840-x (2021).
13 Hadjadj, J. *et al.* Impaired type I interferon activity and inflammatory responses in severe COVID-19 patients. *Science* **369**, 718-724, doi:10.1126/science.abc6027 (2020).
14 Gan, E. S. *et al.* A mouse model of lethal respiratory dysfunction for SARS-CoV-2 infection. *Antiviral Res* **193**, 105138, doi:10.1016/j.antiviral.2021.105138 (2021).
15 Munoz-Fontela, C. *et al.* Animal models for COVID-19. *Nature* **586**, 509-515, doi:10.1038/s41586-020-2787-6 (2020).
16 Chen, R. E. *et al.* In vivo monoclonal antibody efficacy against SARS-CoV-2 variant strains. *Nature* **596**, 103-108, doi:10.1038/s41586-021-03720-y (2021).
17 Johnson, B. A. *et al.* Loss of furin cleavage site attenuates SARS-CoV-2 pathogenesis. *Nature* **591**, 293-299, doi:10.1038/s41586-021-03237-4 (2021).
18 VanBlargan, L. *et al.* A potently neutralizing anti-SARS-CoV-2 antibody inhibits variants of concern by binding a highly conserved epitope. *bioRxiv*, doi:10.1101/2021.04.26.441501 (2021).
19 Winkler, E. S. *et al.* SARS-CoV-2 infection of human ACE2-transgenic mice causes severe lung inflammation and impaired function. *Nat Immunol* **21**, 1327-1335, doi:10.1038/s41590-020-0778-2 (2020).
20 Yinda, C. K. *et al.* K18-hACE2 mice develop respiratory disease resembling severe COVID-19. *PLoS Pathog* **17**, e1009195, doi:10.1371/journal.ppat.1009195 (2021).
21 Zheng, J. *et al.* COVID-19 treatments and pathogenesis including anosmia in K18-hACE2 mice. *Nature* **589**, 603-607, doi:10.1038/s41586-020-2943-z (2021).
22 Graham, J. B. *et al.* Genetic diversity in the collaborative cross model recapitulates human West Nile virus disease outcomes. *mBio* **6**, e00493-00415, doi:10.1128/mBio.00493-15 (2015).
23 Gralinski, L. E. *et al.* Genome Wide Identification of SARS-CoV Susceptibility Loci Using the Collaborative Cross. *PLoS Genet* **11**, e1005504, doi:10.1371/journal.pgen.1005504 (2015).
24 Martin, M. D., Sompallae, R., Winborn, C. S., Harty, J. T. & Badovinac, V. P. Diverse CD8 T Cell Responses to Viral Infection Revealed by the Collaborative Cross. *Cell Rep* **31**, 107508, doi:10.1016/j.celrep.2020.03.072 (2020).
25 Noll, K. E. *et al.* Complex Genetic Architecture Underlies Regulation of Influenza-A-Virus-Specific Antibody Responses in the Collaborative Cross. *Cell Rep* **31**, 107587, doi:10.1016/j.celrep.2020.107587 (2020).
26 Price, A. *et al.* Transcriptional Correlates of Tolerance and Lethality in Mice Predict Ebola Virus Disease Patient Outcomes. *Cell Rep* **30**, 1702-1713 e1706, doi:10.1016/j.celrep.2020.01.026 (2020).
27 Sarkar, S. & Heise, M. T. Mouse Models as Resources for Studying Infectious Diseases. *Clin Ther* **41**, 1912-1922, doi:10.1016/j.clinthera.2019.08.010 (2019).

28 Roberts, A., Pardo-Manuel de Villena, F., Wang, W., McMillan, L. & Threadgill, D. W. The polymorphism architecture of mouse genetic resources elucidated using genome-wide resequencing data: implications for QTL discovery and systems genetics. *Mamm Genome* **18**, 473-481, doi:10.1007/s00335-007-9045-1 (2007).
29 Srivastava, A. *et al.* Genomes of the Mouse Collaborative Cross. *Genetics* **206**, 537-556, doi:10.1534/genetics.116.198838 (2017).
30 Williamson, E. J. *et al.* Factors associated with COVID-19-related death using OpenSAFELY. *Nature* **584**, 430-436, doi:10.1038/s41586-020-2521-4 (2020).
31 Ashbrook, D. G. *et al.* A platform for experimental precision medicine: The extended BXD mouse family. *Cell Syst* **12**, 235-247 e239, doi:10.1016/j.cels.2020.12.002 (2021).
32 Kumari, P. *et al.* Neuroinvasion and Encephalitis Following Intranasal Inoculation of SARS-CoV-2 in K18-hACE2 Mice. *Viruses* **13**, doi:10.3390/v13010132 (2021).
33 Oladunni, F. S. *et al.* Lethality of SARS-CoV-2 infection in K18 human angiotensin-converting enzyme 2 transgenic mice. *Nat Commun* **11**, 6122, doi:10.1038/s41467-020-19891-7 (2020).
34 Francis, M. E. *et al.* SARS-CoV-2 infection in the Syrian hamster model causes inflammation as well as type I interferon dysregulation in both respiratory and non-respiratory tissues including the heart and kidney. *PLoS Pathog* **17**, e1009705, doi:10.1371/journal.ppat.1009705 (2021).
35 Imai, M. *et al.* Syrian hamsters as a small animal model for SARS-CoV-2 infection and countermeasure development. *Proc Natl Acad Sci U S A* **117**, 16587-16595, doi:10.1073/pnas.2009799117 (2020).
36 Tostanoski, L. H. *et al.* Ad26 vaccine protects against SARS-CoV-2 severe clinical disease in hamsters. *Nat Med* **26**, 1694-1700, doi:10.1038/s41591-020-1070-6 (2020).
37 Ackermann, M. *et al.* Pulmonary Vascular Endothelialitis, Thrombosis, and Angiogenesis in Covid-19. *N Engl J Med* **383**, 120-128, doi:10.1056/NEJMoa2015432 (2020).
38 Gupta, A. *et al.* Extrapulmonary manifestations of COVID-19. *Nat Med* **26**, 1017-1032, doi:10.1038/s41591-020-0968-3 (2020).
39 Gu, S. X. *et al.* Thrombocytopathy and endotheliopathy: crucial contributors to COVID-19 thromboinflammation. *Nat Rev Cardiol* **18**, 194-209, doi:10.1038/s41569-020-00469-1 (2021).
40 Bernardes, J. P. *et al.* Longitudinal Multi-omics Analyses Identify Responses of Megakaryocytes, Erythroid Cells, and Plasmablasts as Hallmarks of Severe COVID-19. *Immunity* **53**, 1296-1314 e1299, doi:10.1016/j.immuni.2020.11.017 (2020).
41 Schulte-Schrepping, J. *et al.* Severe COVID-19 Is Marked by a Dysregulated Myeloid Cell Compartment. *Cell* **182**, 1419-1440 e1423, doi:10.1016/j.cell.2020.08.001 (2020).
42 Arunachalam, P. S. *et al.* Systems biological assessment of immunity to mild versus severe COVID-19 infection in humans. *Science* **369**, 1210-1220, doi:10.1126/science.abc6261 (2020).
43 Bost, P. *et al.* Host-Viral Infection Maps Reveal Signatures of Severe COVID-19 Patients. *Cell* **181**, 1475-1488 e1412, doi:10.1016/j.cell.2020.05.006 (2020).
44 Chakraborty, S. *et al.* Proinflammatory IgG Fc structures in patients with severe COVID-19. *Nat Immunol* **22**, 67-73, doi:10.1038/s41590-020-00828-7 (2021).
45 Consiglio, C. R. *et al.* The Immunology of Multisystem Inflammatory Syndrome in Children with COVID-19. *Cell* **183**, 968-981 e967, doi:10.1016/j.cell.2020.09.016 (2020).
46 Mathew, D. *et al.* Deep immune profiling of COVID-19 patients reveals distinct immunotypes with therapeutic implications. *Science* **369**, doi:10.1126/science.abc8511 (2020).
47 Shen, B. *et al.* Proteomic and Metabolomic Characterization of COVID-19 Patient Sera. *Cell* **182**, 59-72 e15, doi:10.1016/j.cell.2020.05.032 (2020).
48 Silvin, A. *et al.* Elevated Calprotectin and Abnormal Myeloid Cell Subsets Discriminate Severe from Mild COVID-19. *Cell* **182**, 1401-1418 e1418, doi:10.1016/j.cell.2020.08.002 (2020).
49 Takahashi, T. *et al.* Sex differences in immune responses that underlie COVID-19 disease outcomes. *Nature* **588**, 315-320, doi:10.1038/s41586-020-2700-3 (2020).
50 Wilk, A. J. *et al.* A single-cell atlas of the peripheral immune response in patients with severe COVID-19. *Nat Med* **26**, 1070-1076, doi:10.1038/s41591-020-0944-y (2020).
51 Blanco-Melo, D. *et al.* Imbalanced Host Response to SARS-CoV-2 Drives Development of COVID-19. *Cell* **181**, 1036-1045 e1039, doi:10.1016/j.cell.2020.04.026 (2020).
52 Zanoni, I. Interfering with SARS-CoV-2: are interferons friends or foes in COVID-19? *Curr Opin Virol* **50**, 119-127, doi:10.1016/j.coviro.2021.08.004 (2021).
53 Ziegler, C. G. K. *et al.* Impaired local intrinsic immunity to SARS-CoV-2 infection in severe COVID-19. *Cell* **184**, 4713-4733 e4722, doi:10.1016/j.cell.2021.07.023 (2021).

54 Niemi, M. E. K. *et al.* Mapping the human genetic architecture of COVID-19. *Nature* **600**, 472-477, doi:10.1038/s41586-021-03767-x (2021).
55 Xiong, H. *et al.* Genomic profiling of collaborative cross founder mice infected with respiratory viruses reveals novel transcripts and infection-related strain-specific gene and isoform expression. *G3 (Bethesda)* **4**, 1429-1444, doi:10.1534/g3.114.011759 (2014).
56 Lilue, J. *et al.* Sixteen diverse laboratory mouse reference genomes define strain-specific haplotypes and novel functional loci. *Nature Genetics* **50**, 1574-1583, doi:10.1038/s41588-018-0223-8 (2018).
57 Phillippi, J. *et al.* Using the emerging Collaborative Cross to probe the immune system. *Genes & Immunity* **15**, 38-46, doi:10.1038/gene.2013.59 (2014).
58 Severe Covid, G. G. *et al.* Genomewide Association Study of Severe Covid-19 with Respiratory Failure. *N Engl J Med* **383**, 1522-1534, doi:10.1056/NEJMoa2020283 (2020).
59 Saichi, M. *et al.* Single-cell RNA sequencing of blood antigen-presenting cells in severe COVID-19 reveals multi-process defects in antiviral immunity. *Nature Cell Biology* **23**, 538-551, doi:10.1038/s41556-021-00681-2 (2021).
60 Collin, R., Balmer, L., Morahan, G. & Lesage, S. Common Heritable Immunological Variations Revealed in Genetically Diverse Inbred Mouse Strains of the Collaborative Cross. *J Immunol* **202**, 777-786, doi:10.4049/jimmunol.1801247 (2019).
61 Rawle, D. J. *et al.* ACE2-lentiviral transduction enables mouse SARS-CoV-2 infection and mapping of receptor interactions. *PLOS Pathogens* **17**, e1009723, doi:10.1371/journal.ppat.1009723 (2021).
62 Fumagalli, V. *et al.* Administration of aerosolized SARS-CoV-2 to K18-hACE2 mice uncouples respiratory infection from fatal neuroinvasion. *Science Immunology* **0**, eabl9929, doi:doi:10.1126/sciimmunol.abl9929.
63 Delorey, T. M. *et al.* COVID-19 tissue atlases reveal SARS-CoV-2 pathology and cellular targets. *Nature* **595**, 107-113, doi:10.1038/s41586-021-03570-8 (2021).

Acknowledgments:

This work was funded by the Division of Intramural Research, National Institutes of Health, National Institute of Allergy and Infectious Diseases. Thank you to the animal caretaker staff at campuses of both RML and The Jackson Laboratory for their work in animal husbandry.

Funding

This work was funded by the Division of Intramural Research, National Institutes of Health, National Institute of Allergy and Infectious Diseases.

Author contributions: Each author's contribution to the paper should be listed [we encourage you to follow the CRediT model]. Each CRediT role should have its own line, and there should not be any punctuation in the initials.

Examples:
Conceptualization: SB, NR, SMH
Methodology: SJR, NR, SB
Investigation: SJR, OB, KLM, ML, CC, CB, CS, RMB, AIC, GLS, EF, CP, SM
Visualization: SJR, CNB, JH, DES, CM
Funding acquisition: SB and NR
Supervision: SB and NR
Writing – original draft: SB, SJR, CB, NR
Writing – review & editing: SB, SJR, CB, NR

615
616 **Competing interests:**

617 The authors have no competing interests to declare.

618 **Data and materials availability:** All data, code, and materials used in the analysis must be available in some form
619 to any researcher for purposes of reproducing or extending the analysis. Include a note explaining any
620 restrictions on materials, such as materials transfer agreements (MTAs). Note accession numbers to any
621 data relating to the paper and deposited in a public database; include a brief description of the data set or
622 model with the number. If all data are in the paper and supplementary materials, include the sentence "All
623 data are available in the main text or the supplementary materials."

624
625

626 **Figure Legends:**

627

628 **Figure 1: CCxK18-hACE2 F1 progeny mice demonstrate a range of clinical severity following infection with**
629 **SARS-CoV-2.** Mice were infected intranasally with 10^3PFU of SARS-CoV-2 and monitored for survival and weight
630 loss. F1 founder strains were classified as: (**A)** sensitive with 50% or greater mortality and no difference between
631 males and females, **(B)** resistant with 35% or less mortality, or **(C)** sensitive with a sex bias as having statistically
632 significant difference between sensitivity of male and female mice. Mice without evidence of seroconversion at the
633 end of the study were removed from analysis (N=6-8/per sex).

634

635 **Figure 2: Virus replication kinetics and pathology in CCxK18-hACE2 F1 progeny.** (**A)** Virus titers (PFU/g
636 tissue) in lung and brain of male and female mice were measured at 3 and 6 dpi. (**B)** RNAscope of SARS-CoV-2
637 genome predominantly localizing to pneumocytes in areas of lung inflammation. Serial sections demonstrate
638 pathology (upper) and viral RNA distribution (lower; Red). Scale bars represent 100mm. (**C)** Examples of pathology
639 scoring used in this study. Scale bars represent 500mm. (**D),** Lung pathology scores for CC Founder F1 males and
640 females at 3 and 6 dpi. N = 6/time point/sex.

641

642 **Figure 3: Timing of type I IFN and inflammatory cytokine responses in the lung is associated with clinical**
643 **severity in CCxK18-hACE2 F1 progeny.** (**A)** IFNα protein in BAL from CCxK18-hACE2 F1 progeny at 3 dpi.
644 IFNα protein in BAL from **(B)** male and **(C)** female resistant (PWK, NZO and 129S1 x K18-hACE2) and sensitive
645 (K18-hACE2 and A/J x K18-hACE2) mice at 3 and 6 dpi. **(D)** Heatmap of cytokine and chemokine responses in

646 BAL. **(E)** Resolving group A cytokines in F1 progeny resistant to lethality (blue box), increasing group B cytokines
647 in sensitive F1 progeny. Correlation plots for K18-hACE2 and PWK x K18-hACE2 at **(F)** 3 dpi and **(G)** 6 dpi.
648
649 **Supplemental Figure 1: Survival, weight loss and SARS-CoV-2 replication kinetics in BALB/cxK18-hACE2**
650 **or DBAxK18-hACE2 F1 progeny.** (**A)** Survival and weight loss in BALB/cxK18-hACE2 F1. (**B)** Survival and
651 weight loss in DBA x K18-hACE2 F1. (**C)** Virus titers (PFU/g tissue) in lung and brain of male and female mice
652 were measured at 3 and 6 dpi. (**D)** Heatmap of cytokine expression in BAL.
653
654 **Supplemental Figure 2: Relative expression of human *ACE2* in lungs of CCxK18-hACE2 F1 progeny.** Gene
655 expression was measured by real-time RT-PCR and expressed relative to that in male and female K18-hACE2 mice.
656
657 **Supplemental Figure 3: Examples of pathology in the brain of SARS-CoV-2-infected CCxK18-hACE2 F1**
658 **progeny.** (**A)** Small focal areas of inflammation were commonly observed (circled). Scale bar = 1000mm. (**B)**
659 increased magnification of (A) demonstrating perivascular cuffing, gliosis, and evidence of necrotic cells in areas of
660 focal inflammation. Scale bar = 200mm. (**C)** Example of a pronounced lymphocytic inflammatory response with
661 perivascular cuffing and increased cellularity (arrowheads). Scale bar = 100mm. (**D)** Microthrombus occluding
662 cerebral capillaries and hemorrhage (arrow) observed in CASTxK18-hACE2. Scale bar = 100mm. (**E)** Example of
663 extensive hemorrhage in the brain of CASTxK18-hACE2 F1 progeny associated with extensive virus replication as
664 demonstrated in F. Scale bar = 1000mm. (**F)** serial section relative to (E) showing extensive SARS-CoV-2 genome
665 by RNAscope. Scale bar = 1000mm. (**G)** Incidence of encephalitis for CC Founder F1 males and females at 3 and 6
666 dpi.
667
668 **Supplemental Figure 4: Interferon, cytokine and chemokine expression in the serum compared to the BAL of**
669 **SARS-CoV-2-infected CCxK18-hACE2 F1 progeny.** Heatmap showing relative cytokine levels, as measured by
670 multiplex cytokine assays, for all eight at CCxK18-hACE2 F1s at (**A)** 3 dpi, and (**B)** 6 dpi, and (**C)** for strains with a
671 sex-bias at 3 and 6 dpi.
672

673 **Supplemental Figure 5: Interferon, cytokine and chemokine expression in the BAL from SARS-CoV-2-**
674 **infected sensitive and resistant CCxK18-hACE2 F1 progeny.** Cytokines were measured at 3 and 6 dpi by
675 multiplex cytokine assays. Graphs represent data from male and female sensitive (K18-hACE2 and A/J x K18-
676 hACE2) and resistant (PWK, NZO and 129S1J x K18-hACE2) F1s. **(A)** "Group A" cytokines with higher
677 production in resistant F1 progeny compared to sensitive F1 progeny at 3 dpi. The average cytokine expression in
678 BAL of naïve mice is indicated by a grey dashed line.
679
680 **Supplemental Figure 6: Interferon, cytokine and chemokine expression in the serum from SARS-CoV-2-**
681 **infected sensitive and resistant CCxK18-hACE2 F1 progeny.** Cytokines were measured at 3 and 6 dpi by
682 multiplex cytokine assays. Graphs represent data from male and female sensitive (K18-hACE2 and A/J x K18-
683 hACE2) and resistant (PWK, NZO and 129S1J x K18-hACE2) F1s. **(A)** "Group A" cytokines with higher
684 production in resistant F1 progeny compared to sensitive F1 progeny at 3 dpi. The average cytokine expression in
685 BAL of naïve mice is indicated by a grey dashed line.
686
687 **Supplemental Figure 7: Interferon, cytokine and chemokine expression in the BAL from SARS-CoV-2-**
688 **infected CCxK18-hACE2 F1 with a sex bias.** Graphs show cytokine levels in male versus female for CAST,
689 NOD, and WSB x K18-hACE2 F1. Cytokines were measured at 3 and 6 dpi by multiplex cytokine assays. The
690 average cytokine expression in BAL of naïve mice is indicated by a grey dashed line.
691
692 **Table S1.** Summary of percent survival, weight loss, virus burden and BAL cytokine profiles in K18-hACE2 x CC
693 Founder F1 progeny.
694
695 **Table S2.** Summary of statistical analyses of cytokine and chemokine expression in BAL fluid collected from
696 resistant and sensitive K18-hACE2 x CC Founder F1 progeny.
697
698 **Table S3.** Summary of statistical analyses of cytokine and chemokine expression in BAL fluid comparing male and
699 female resistant PWK x K18-hACE2 and sensitive K18-hACE2 x CC Founder F1 progeny.
700

Table S1

				Peak weight loss		Average Virus Titers in Lung		Cytokine profile BAL	
Strain (F1)	Sex	%Survival	Mean time to death (days)	%	DPI	3 dpi Mean (Std Dev)	6 dpi Mean (Std Dev)	3 dpi	6 dpi
C57Bl/6 x K18-hACE2	M	14	6	16.7	7	1.3e6 (1.8e6)	7.6e4 (1.3e5)	No/Low	High Group A and Group B
	F	29	7	12.0	7	1.5e6 (1.4e6)	8.2e3 (5.7e3)		
A/J x K18-hACE2	M	33	8	15.0	7	2.8e6 (2.2e6)	3.5e4 (6.1e4)	No/Low	High Group A and Group B
	F	66	UD	6.1	7	2.8e6 (2.6e6)	2.7e4 (2.8e4)		
PWK x K18-hACE2	M	83	UD	-	-	1.6e5 (2.3e5)	BLD	High Group A	Moderate Group A and Group B
	F	83	UD	7.0	7	9.2e4 (1.1e4)	BLD		
NZO x K18-hACE2	M	86	UD	13.9	9	2.2e6 (2.8e6)	3.8e3 (3.7e3)	High Group A	High Group A and B
	F	71	UD	21.9	9	1.4e6 (1.2e6)	1.3e3 (1.0e3)		
129S1 x K18-ACE2	M	86	UD	11.8	7	1.3e6 (7.8e5)	3.0e3 (2.8e3)	High Group A	High Group A and Group B
	F	71	UD	12.0	7	8.1e5 (6.4e4)	2.4e4 (4.0e4)		
CAST/EiJ x K18-ACE2	M	0	6	17.2	7	6.7e6 (7.1e6)	4.2e5(3.5e5)	Low Group A	Low Group A
	F	50	15.5	35.8	8	1.6e6(1.4e6)	3.4e4 (2.9e4)	Low Group A	Low Group A
NOD x K18-ACE2	M	33	6.5	6.0	6	2.5e6 (4.4e6)	4.8e3 (5.3e3)	No/Low	Moderate I and II
	F	83	UD	-	-	5.1e5 (7.9e5)	6.4e3 (8.1e3)	No/Low	Moderate I and II
WSB x K18-ACE2	M	66	UD	32.0	11	4.1e6 (1.8e6)	3.1e4 (1.6e4)	Moderate Group A	High Group A and B
	F	0	8	25.1	8	4.4e6 (4.1e6)	2.5e4 (1.2e4)	Moderate Group A	Moderate Group A and Group B
BALB/c x K18-ACE2	M	100	UD	3.0	5	6.0e5 (5.5e5)	1.6e4 (1.3e4)	No/Low	Low Group B
	F	66	UD	8.3	6	3.7e5 (4.2e5)	6.0e2 (1.2e3)	High Group A	High Group A and Group B
DBA/2 x K18-ACE2	M	57	UD	16.0	10	1.5e6 (1.7e6)	1.7e4 (2.2e4)	No/Low	No/Low
	F	71	UD	3.6	6	1.7e6 (1.2e6)	1.2e3 (1.0e3)	No/Low	High Group A and Group B

UD: undetermined
BLD: below limit of detection

743
744 Table S2

	Resistant[1] versus Sensitive[2]		**Kinetics**	
	R>S[3]	S>R[4]	**3 dpi versus 6 dpi[5]**	
	3 dpi	**6 dpi**	**Resistant[1]**	**Sensitive[2]**
Analyte	**P value**	**P value**	**P value**	**P value**
GM-CSF	8.7e-02	2.4e-01	2.4e-01	**1.3e-03**
IFNalpha	**2.9e-05**	1.8e-01	**1.4e-12**	**7.1e-04**
IFNgamma	**1.1e-03**	5.1e-01	**1.9e-05**	**1.3e-03**
IL1-beta	**2.2e-02**	4.1e-01	**1.7e-02**	**1.3e-03**
IL-12p70	**2.1e-03**	1.0e-01	1.0e-00	**1.2e-02**
IL-13	**1.7e-03**	4.6e-01	**1.2e-03**	**2.2e-04**
IL-18	**1.7e-03**	4.7e-01	**1.2e-04**	**1.2e-04**
IL-2	6.4e-01	6.4e-01	**2.5e-03**	**8.8e-04**
IL-4	5.1e-02	5.2e-01	**7.5e-03**	**1.2e-03**
IL-5	8.8e-01	8.8e-01	**5.7e-03**	**4.2e-03**
IL-6	**1.0e-02**	2.4e-01	**7.7e-06**	8.6e-01
TNFα	**3.9e-03**	2.0e-01	9.1e-02	**2.2e-03**
IL-10	6.7e-01	**1.9e-02**	**1.2e-06**	**1.2e-03**
*IL-17A	**1.7e-02**	5.8e-01	**1.7e-02**	6.8e-01
IL-22	**8.3e-03**	1.0e-01	7.9e-01	5.2e-02
IL-23	8.1e-01	9.4e-01	3.2e-01	3.8e-01
IL-27	**2.9e-03**	8.2e-01	**4.1e-02**	4.7e-01
*IL-9	1.0e-00	1.0e-01	4.6e-01	5.1e-01
Eotaxin	**2.0e-02**	7.2e-01	**3.9e-03**	**7.8e-04**
Gro-alpha/KC	**3.0e-03**	2.1e-01	7.9e-01	1.5e-01
CCL2 (MCP1)	**2.5e-03**	6.1e-01	5.5e-02	1.3e-01
CCL3 (MIP1a)	**2.4e-02**	3.1e-01	5.7e-01	**4.8e-04**
CCL4 (MIP1b)	**1.1e-03**	**4.1e-02**	3.0e-01	**1.1e-03**
CCL5 (RANTES)	7.9e-02	6.2e-01	1.3e-01	**3.7e-03**
CCL7 (MCP3)	**1.5e-02**	8.6e-01	9.3e-01	**4.5e-03**
CXCL2 (MIP2a)	**3.7e-03**	4.2e-01	5.8e-02	6.6e-02
CXCL10 (IP10)	**6.4e-03**	6.3e-01	**6.4e-03**	3.4e-01

745
746 *At or below the lower limit of detection
747 [1] Resistant mice include PWK, NZO and 129S1 x K18-hACE2 F1 progeny
748 [2] Sensitive mice include K18-hACE2 and A/J x K18-hACE2 F1 progeny
749 [3] Higher levels of analytes in resistant compared to sensitive
750 [4] Higher levels of analytes in sensitive compared to resistant
751 [5] Bold black text indicates statistically significant increase from 3 dpi to 6 dpi. Bold blue text
752 indicates statistically significant decrease from 3 dpi to 6 dpi.
753
754

755
756 Table S3

	PWK[1] vs B6[2]	PWK vs B6	PWK vs B6	PWK vs B6
	Females		**Males**	
	3 dpi	**6 dpi**	**3 dpi**	**6 dpi**
Analyte	**P value**	**P value**	**P value**	**P value**
GM-CSF	**9.8e-04**	**8.1e-04**	3.4e-01	1.1e-01
IFNalpha	**6.4e-03**	ND	**3.3e-06**	ND
IFNgamma	**5.2e-04**	1.9e-01	**2.8e-03**	3.3e-01
IL1-beta	**6.0e-04**	**4.9e-03**	1.2e-01	2.0e-01
IL-12p70	6.1e-02	**4.9e-02**	**2.7e-03**	4.4e-01
IL-13	**8.9e-06**	**9.8e-03**	9.7e-02	2.4e-01
IL-18	**1.1e-04**	**8.0e-03**	**3.3e-02**	2.0e-01
IL-2	9.7e-02	9.8e-02	9.0e-01	3.1e-01
IL-4	**1.9e-03**	**3.0e-03**	4.1e-01	1.3e-01
IL-5	1.2e-01	**9.6e-03**	9.5e-01	1.6e-01
IL-6	**4.8e-02**	**4.8e-02**	**3.8e-03**	4.4e-01
TNFα	**4.3e-02**	**1.2e-03**	5.4e-02	2.3e-01
IL-10	**5.3e-03**	**2.9e-03**	6.4e-01	1.9e-01
*IL-17A	**2.3e-03**	**1.6e-02**	4.1e-01	6.8e-01
IL-22	**5.2e-03**	9.7e-01	**1.1e-02**	5.2e-01
IL-23	2.1e-01	2.2e-01	3.0e-01	**5.3e-03**
IL-27	6.6e-01	9.7e-01	**8.0e-04**	4.0e-01
*IL-9	7.4e-01	ND	2.2e01	ND
Eotaxin	5.4e-01	**1.3e-03**	8.5e-02	2.0e-01
Gro-alpha/KC	**7.2e-03**	**1.8e-05**	**2.2e-03**	7.6e-02
CCL2 (MCP1)	6.1e-02	**1.4e-02**	**2.2e-03**	3.2e-01
CCL3 (MIP1a)	4.9e-01	**1.8e-02**	**9.8e-03**	7.6e-02
CCL4 (MIP1b)	**6.7e-03**	**1.0e-06**	**1.9e-03**	5.6e-02
CCL5 (RANTES)	8.6e-01	**1.8e-02**	6.0e-02	3.1e-01
CCL7 (MCP3)	**1.3e-02**	**6.5e-03**	8.0e-02	**3.0e-02**
CXCL2 (MIP2a)	**3.6e-03**	1.2e-01	**4.3e-02**	**2.8e-02**
CXCL10 (IP10)	**1.2e-04**	4.9e-01	**3.2e-02**	**7.2e-03**

757
758
759 *At or below the lower limit of detection
760 [1] Resistant mice include PWK x K18-hACE2 F1 progeny
761 [2] Sensitive mice include K18-hACE2 (C57Bl/6J (B6) background)
762 Bold black text indicates statistically significance for higher production in PWK than B6.
763 Bold blue text indicates statistically significance for lower production in PWK than B6.

A Sensitive

C57Bl/6JxK18-hACE2

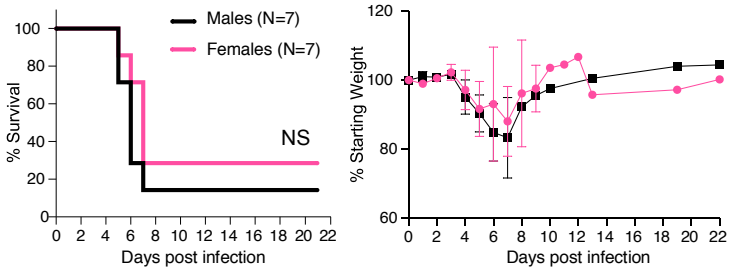

A/JxK18-hACE2

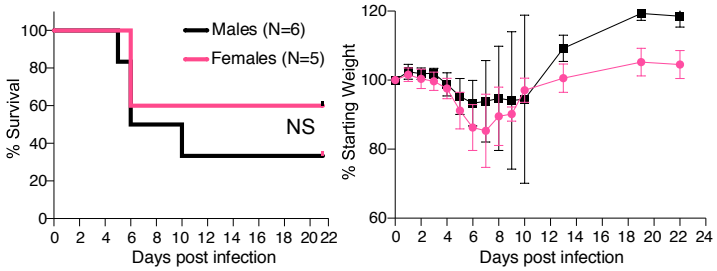

B Resistant

PWKxK18-hACE2

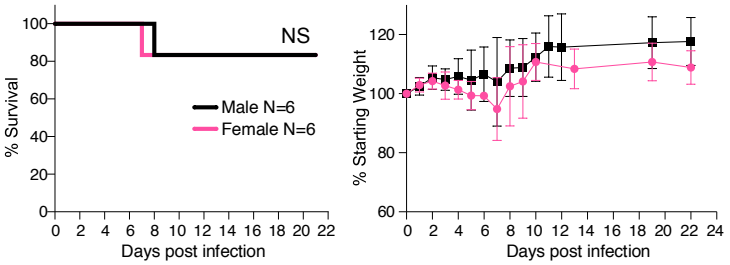

NZOxK18-hACE2

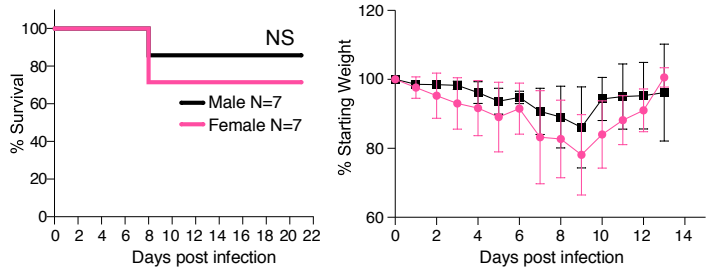

129S1xK18-hACE2

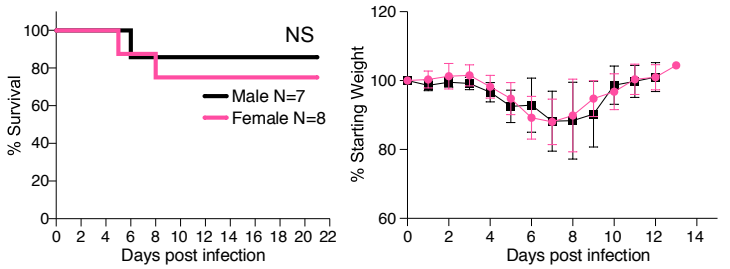

C Sensitive with Sex Bias

CASTxK18-hACE2

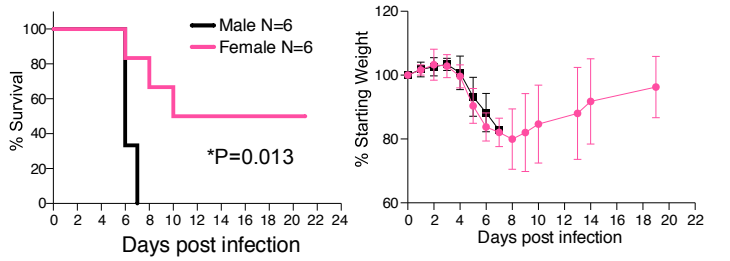

NODxK18-hACE2

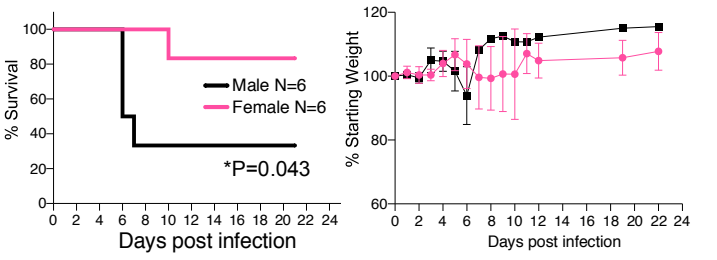

WSBxK18-hACE2

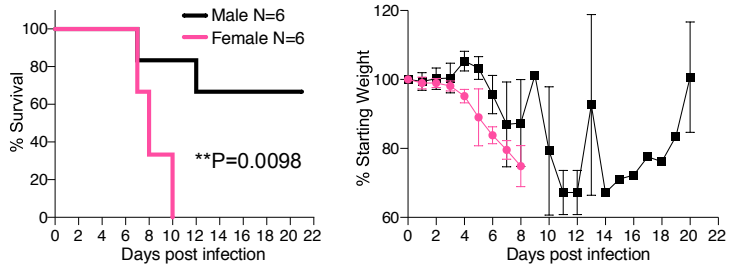

Figure 1 12.13.21

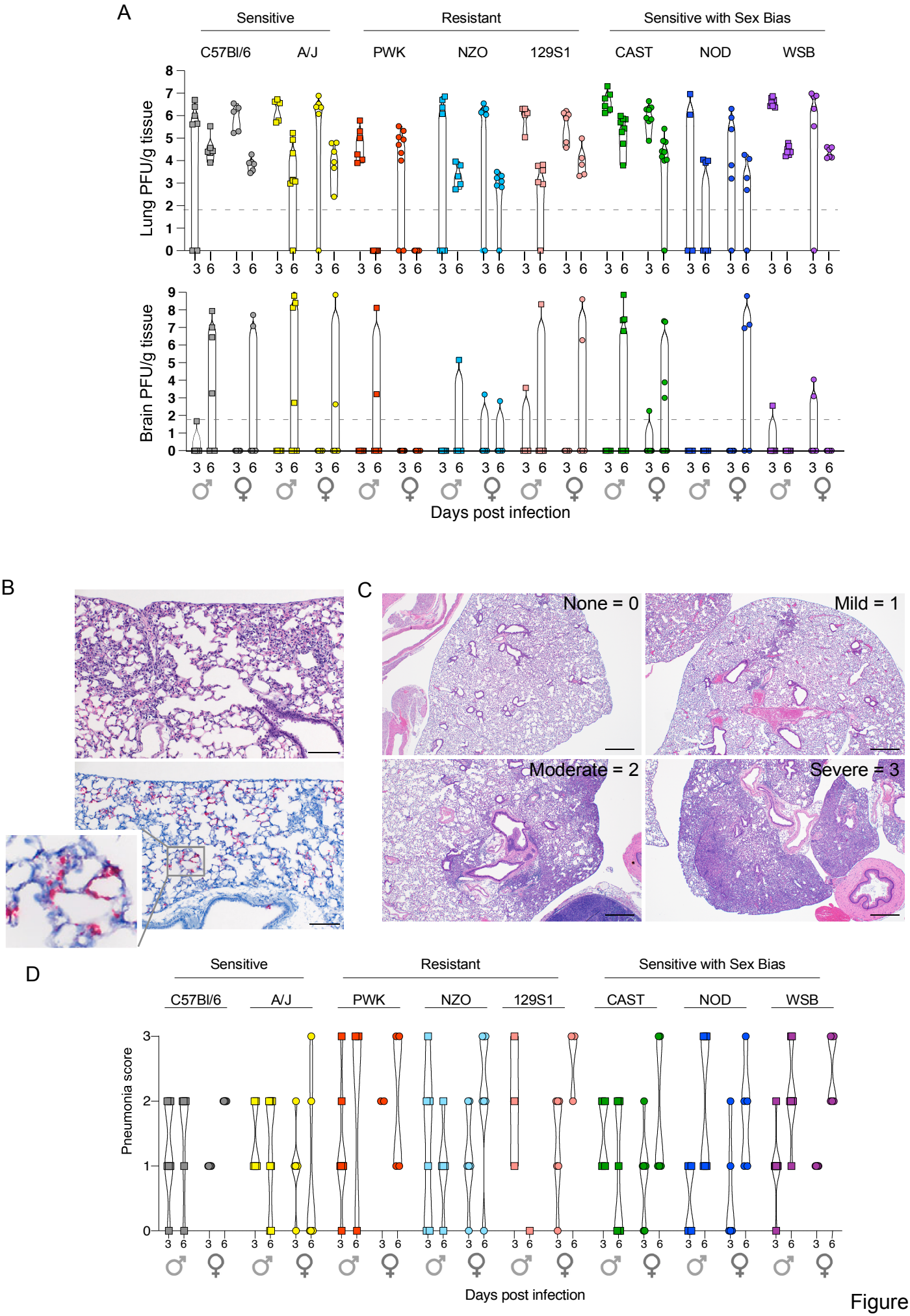
A
Sensitive
Resistant
Sensitive with Sex Bias
C57Bl/6
A/J
PWK
NZO
129S1
CAST
NOD
WSB
Lung PFU/g tissue
Brain PFU/g tissue
Days post infection
B
C
None = 0
Mild = 1
Moderate = 2
Severe = 3
D
Pneumonia score
Days post infection

Figure 2

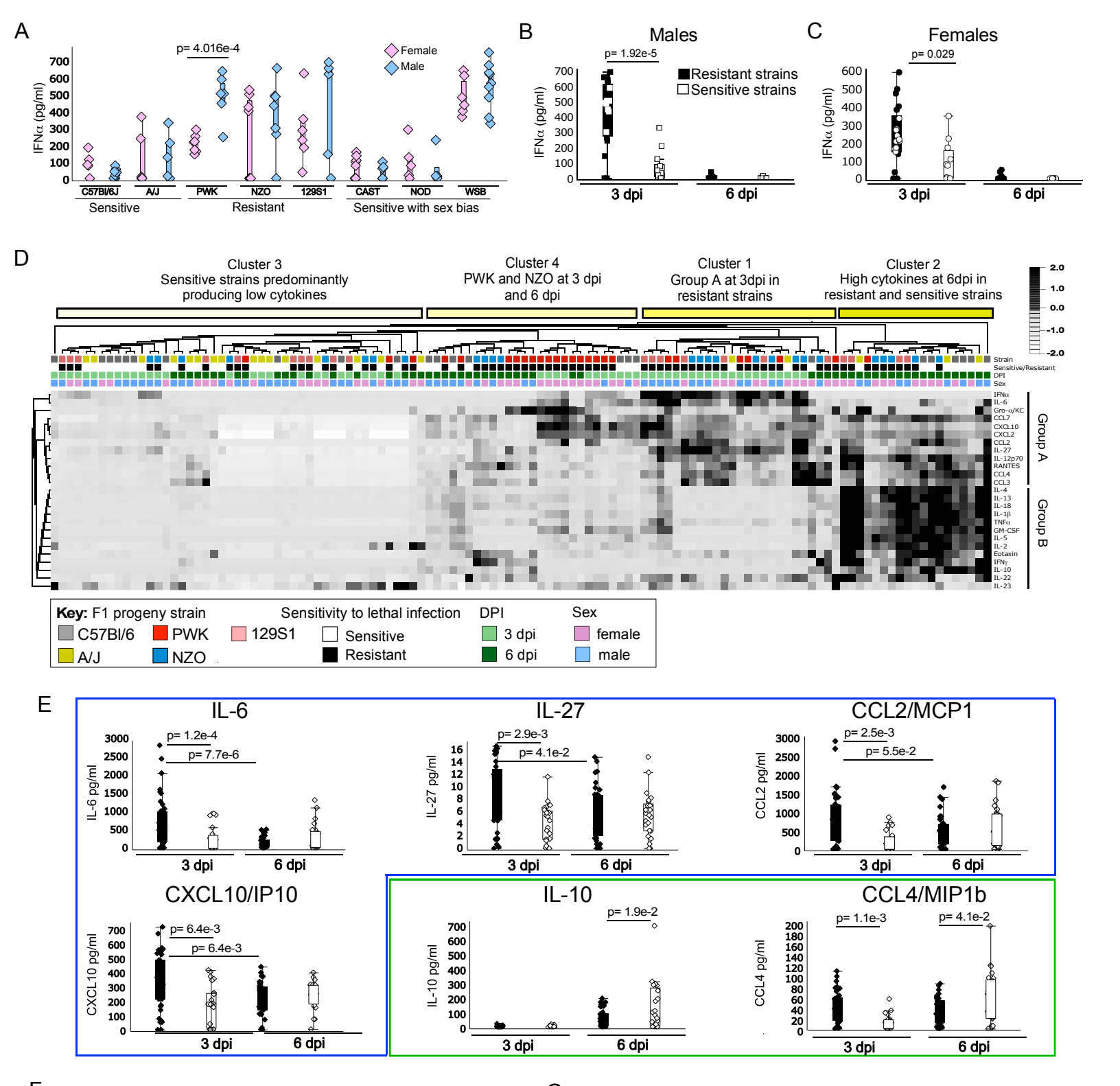
A
p= 4.016e-4
Female
Male
IFNα (pg/ml)
C57Bl/6J
A/J
PWK
NZO
129S1
CAST
NOD
WSB
Sensitive
Resistant
Sensitive with sex bias
B
Males
p= 1.92e-5
Resistant strains
Sensitive strains
3 dpi
6 dpi
C
Females
p= 0.029
D
Cluster 3
Sensitive strains predominantly producing low cytokines
Cluster 4
PWK and NZO at 3 dpi and 6 dpi
Cluster 1
Group A at 3dpi in resistant strains
Cluster 2
High cytokines at 6dpi in resistant and sensitive strains
Strain
Sensitive/Resistant
DPI
Sex
Group A
Group B
Key: F1 progeny strain
C57Bl/6
PWK
129S1
A/J
NZO
Sensitivity to lethal infection
Sensitive
Resistant
DPI
3 dpi
6 dpi
Sex
female
male
E
IL-6
p= 1.2e-4
p= 7.7e-6
IL-6 pg/ml
IL-27
p= 2.9e-3
p= 4.1e-2
IL-27 pg/ml
CCL2/MCP1
p= 2.5e-3
p= 5.5e-2
CCL2 pg/ml
CXCL10/IP10
p= 6.4e-3
p= 6.4e-3
CXCL10 pg/ml
IL-10
p= 1.9e-2
IL-10 pg/ml
CCL4/MIP1b
p= 1.1e-3
p= 4.1e-2
CCL4 pg/ml
F
B6xK18–hACE2 3 DPI
PWKxK18–hACE2 3 DPI
G
B6xK18–hACE2 6 DPI
PWKxK18–hACE2 6 DPI
value

Figure 3

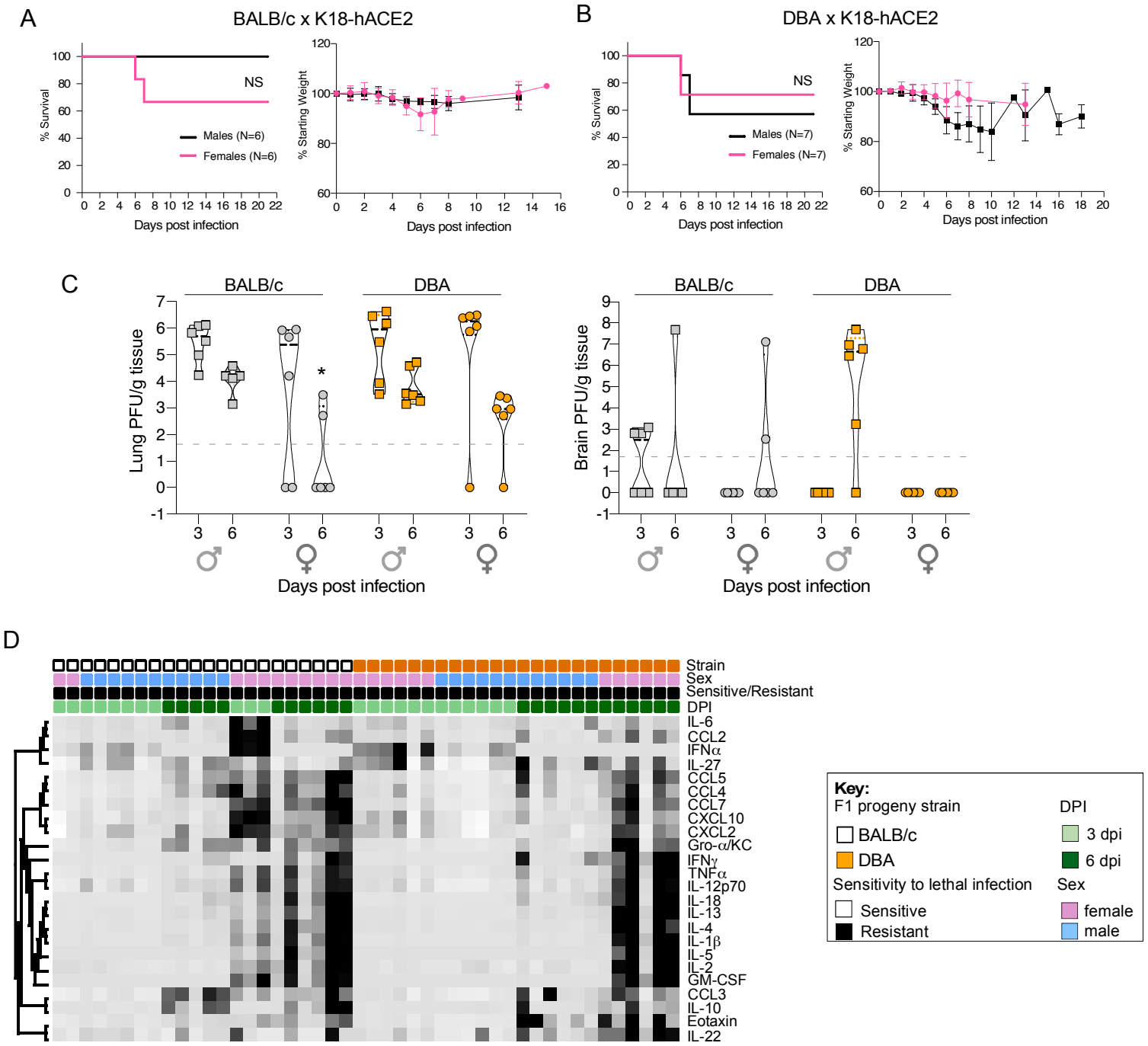
A
BALB/c x K18-hACE2
% Survival
NS
Males (N=6)
Females (N=6)
Days post infection
% Starting Weight
Days post infection
B
DBA x K18-hACE2
% Survival
NS
Males (N=7)
Females (N=7)
Days post infection
% Starting Weight
Days post infection
C
BALB/c
DBA
Lung PFU/g tissue
Days post infection
BALB/c
DBA
Brain PFU/g tissue
Days post infection
D
Strain
Sex
Sensitive/Resistant
DPI
IL-6
CCL2
IFNα
IL-27
CCL5
CCL4
CCL7
CXCL10
CXCL2
Gro-α/KC
IFNγ
TNFα
IL-12p70
IL-18
IL-13
IL-4
IL-1β
IL-5
IL-2
GM-CSF
CCL3
IL-10
Eotaxin
IL-22
Key:
F1 progeny strain
BALB/c
DBA
Sensitivity to lethal infection
Sensitive
Resistant
DPI
3 dpi
6 dpi
Sex
female
male

Fig. S1

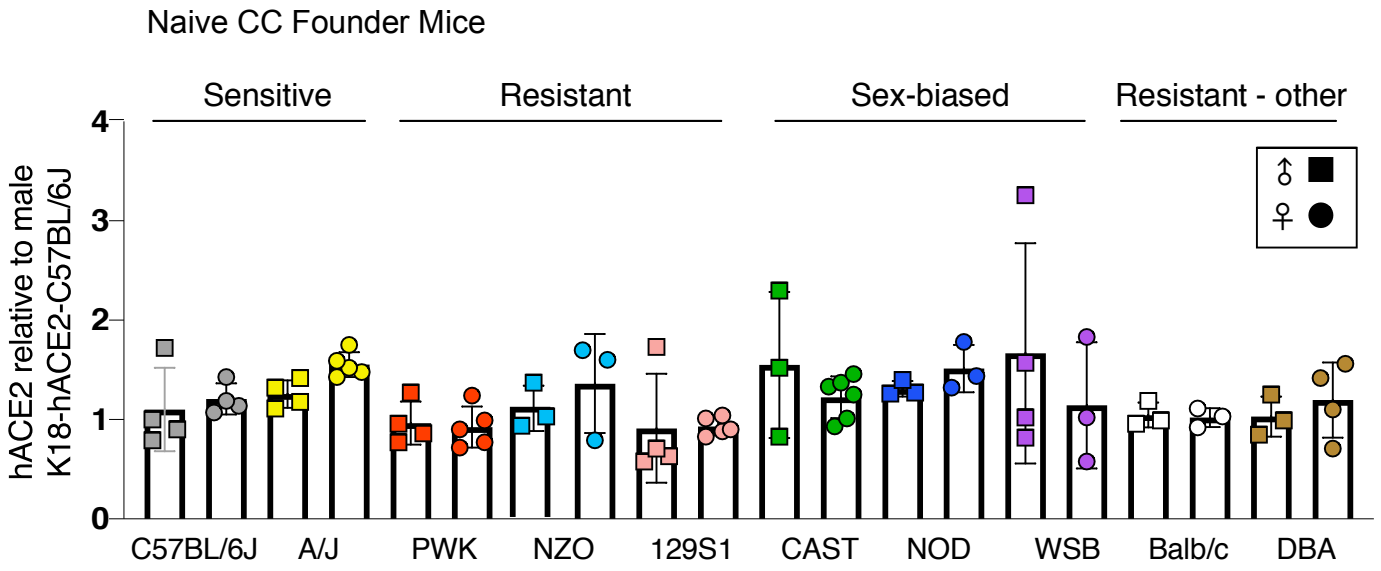
Naive CC Founder Mice
Sensitive
Resistant
Sex-biased
Resistant - other
hACE2 relative to male
K18-hACE2-C57BL/6J
0
1
2
3
4
♂
♀
C57BL/6J
A/J
PWK
NZO
129S1
CAST
NOD
WSB
Balb/c
DBA

Fig. S2

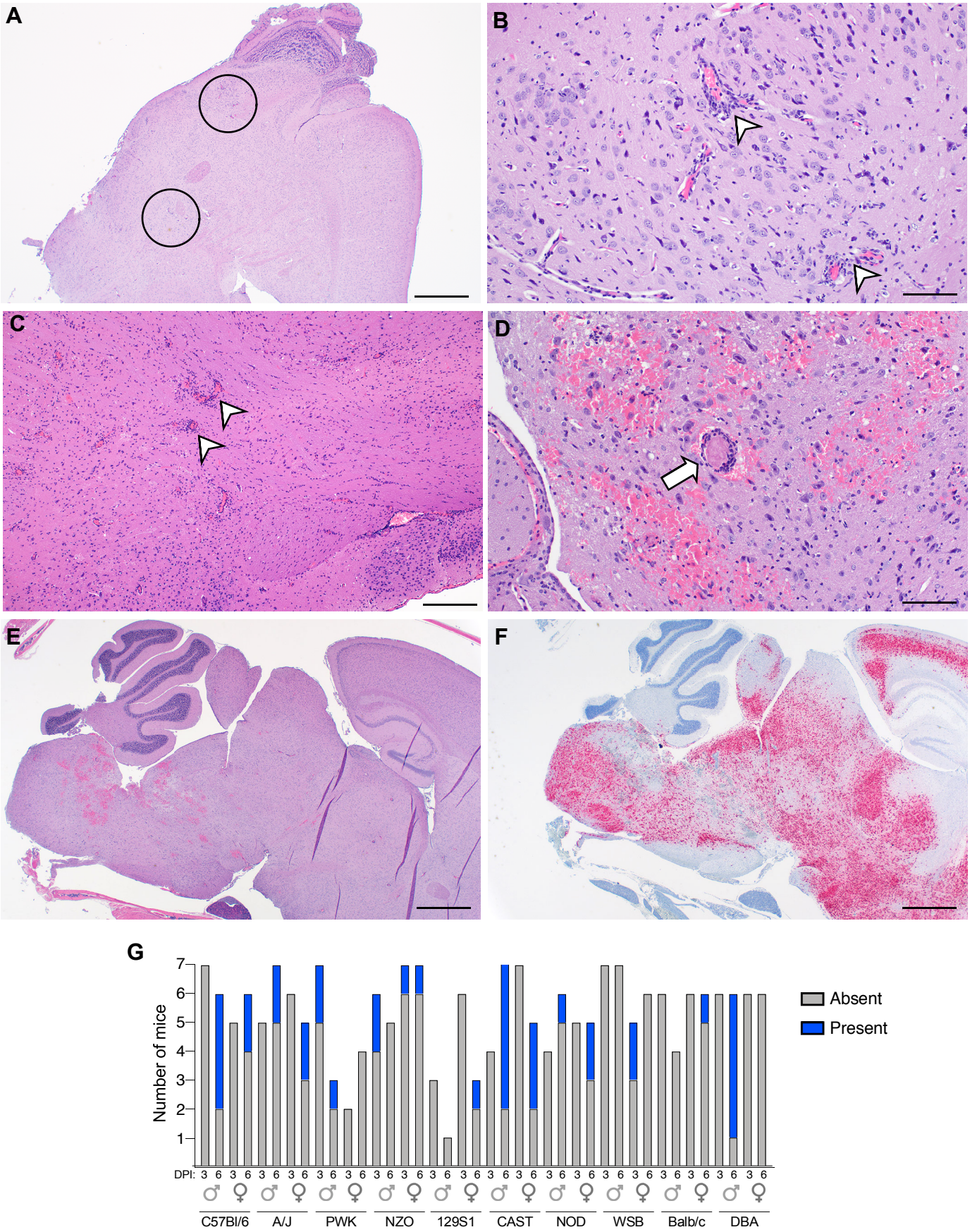
A
B
C
D
E
F
G
Number of mice
7
6
5
4
3
2
1
DPI: 3 6 3 6 3 6 3 6 3 6 3 6 3 6 3 6 3 6 3 6 3 6 3 6 3 6 3 6 3 6 3 6 3 6 3 6 3 6
♂ ♀ ♂ ♀ ♂ ♀ ♂ ♀ ♂ ♀ ♂ ♀ ♂ ♀ ♂ ♀ ♂ ♀ ♂ ♀
C57Bl/6
A/J
PWK
NZO
129S1
CAST
NOD
WSB
Balb/c
DBA
Absent
Present

Fig. S3

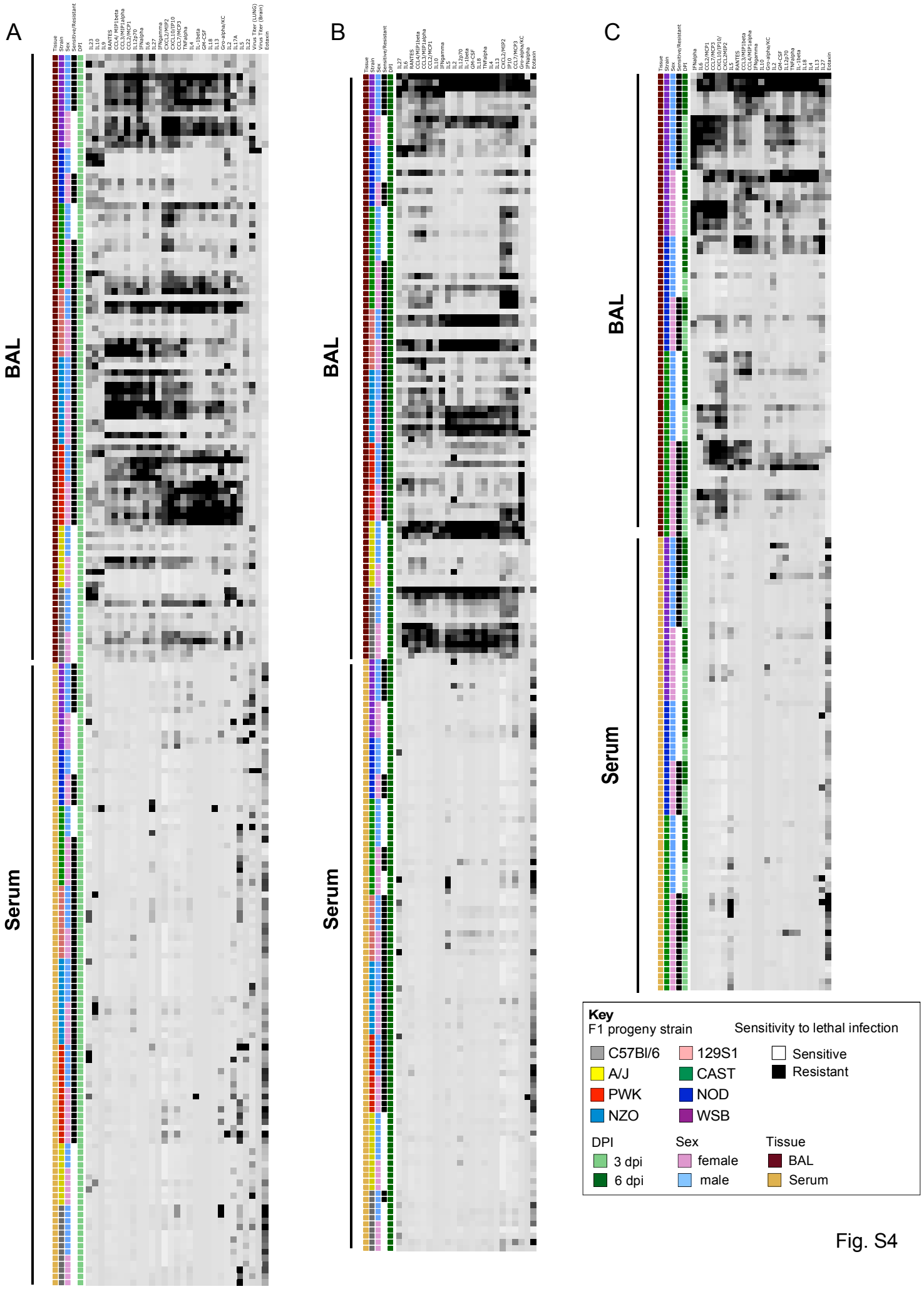
A
B
C
BAL
Serum
Tissue
Strain
Sex
Sensitive/Resistant
DPI
Key
F1 progeny strain
C57Bl/6
129S1
A/J
CAST
PWK
NOD
NZO
WSB
Sensitivity to lethal infection
Sensitive
Resistant
DPI
3 dpi
6 dpi
Sex
female
male
Tissue
BAL
Serum

Fig. S4

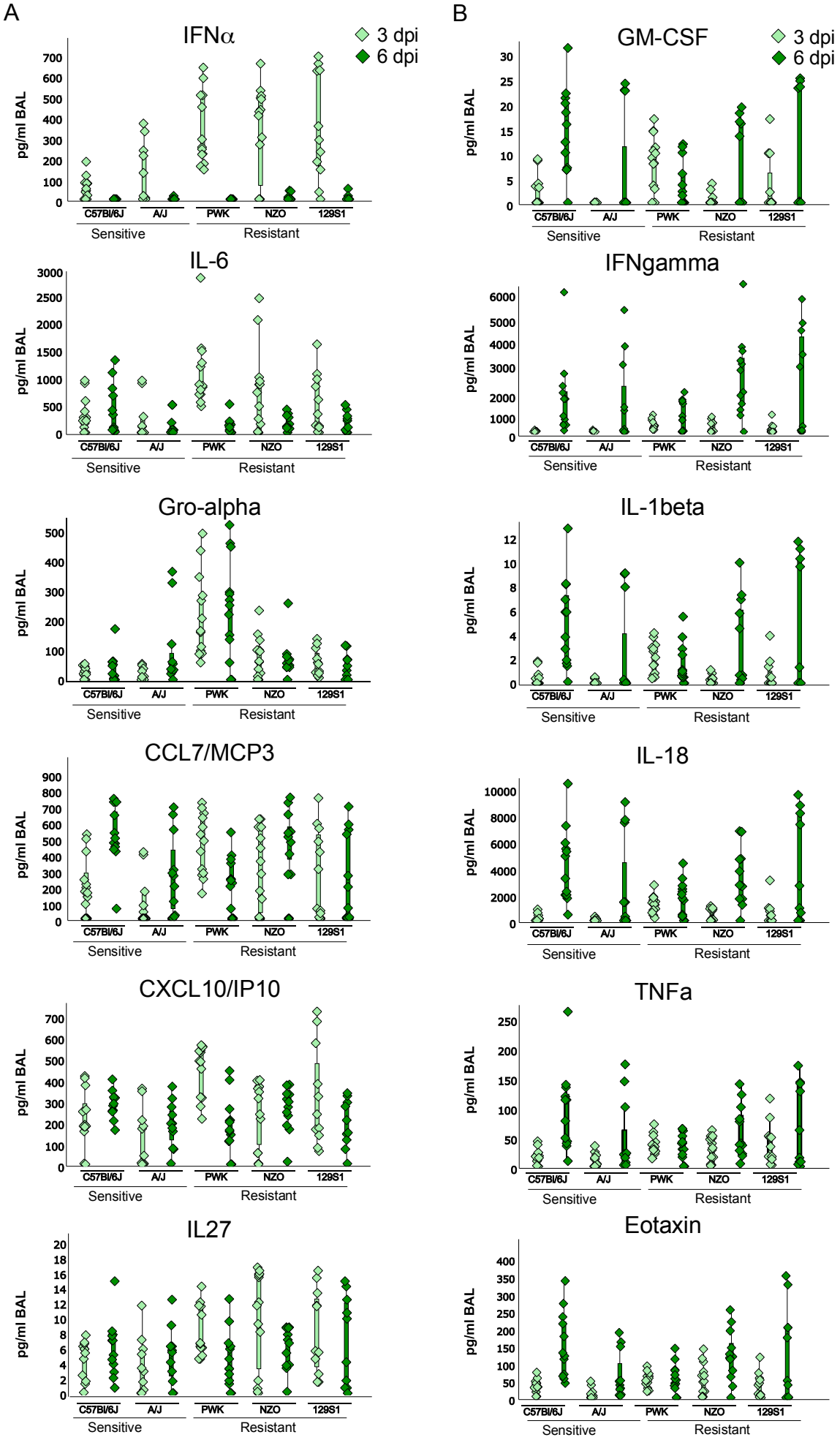
A
B
IFNα
GM-CSF
3 dpi
6 dpi
pg/ml BAL
C57Bl/6J
A/J
PWK
NZO
129S1
Sensitive
Resistant
IL-6
IFNgamma
Gro-alpha
IL-1beta
CCL7/MCP3
IL-18
CXCL10/IP10
TNFa
IL27
Eotaxin

Fig. S5

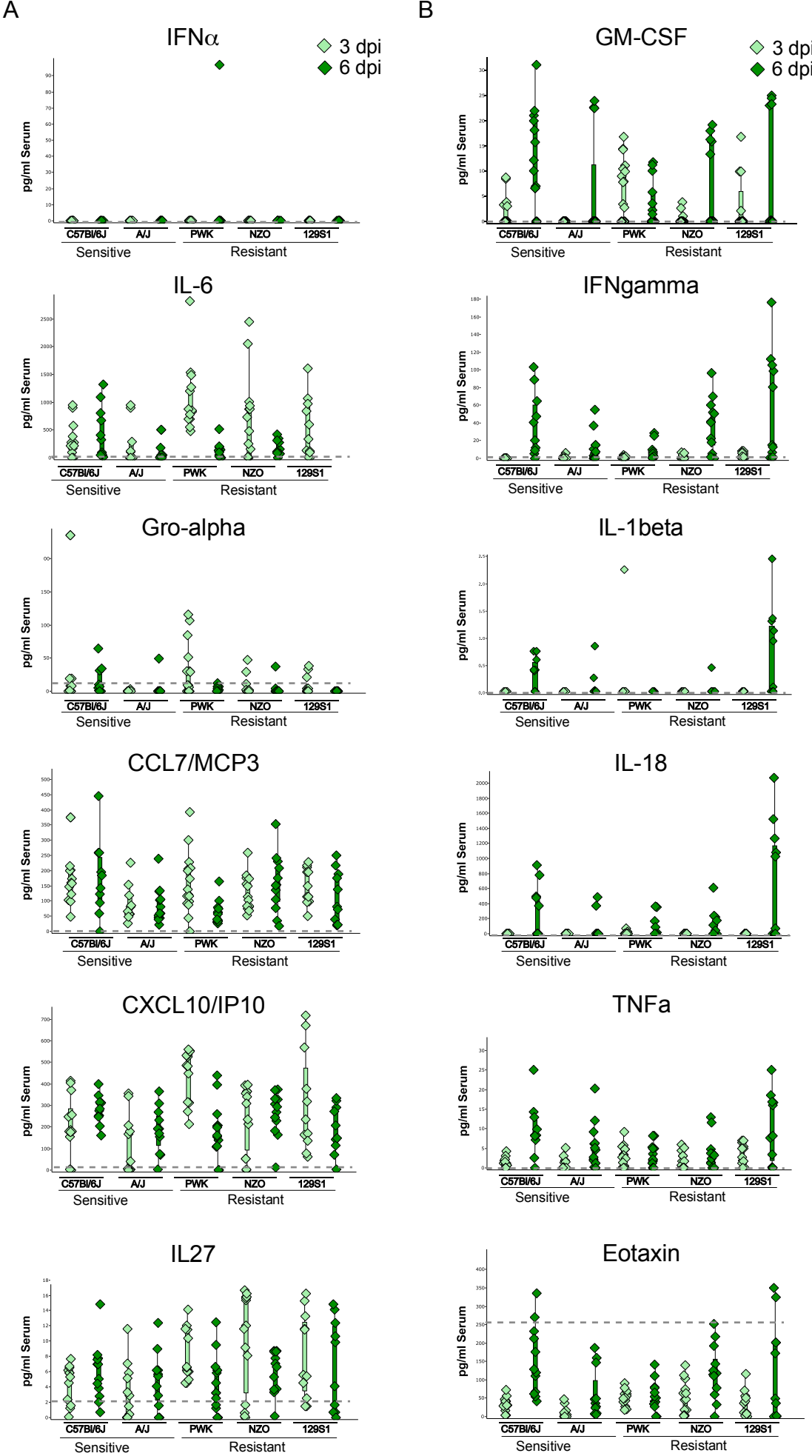
A
B
IFNα
GM-CSF
IL-6
IFNgamma
Gro-alpha
IL-1beta
CCL7/MCP3
IL-18
CXCL10/IP10
TNFa
IL27
Eotaxin
3 dpi
6 dpi
pg/ml Serum
C57Bl/6J
A/J
PWK
NZO
129S1
Sensitive
Resistant

Fig. S6

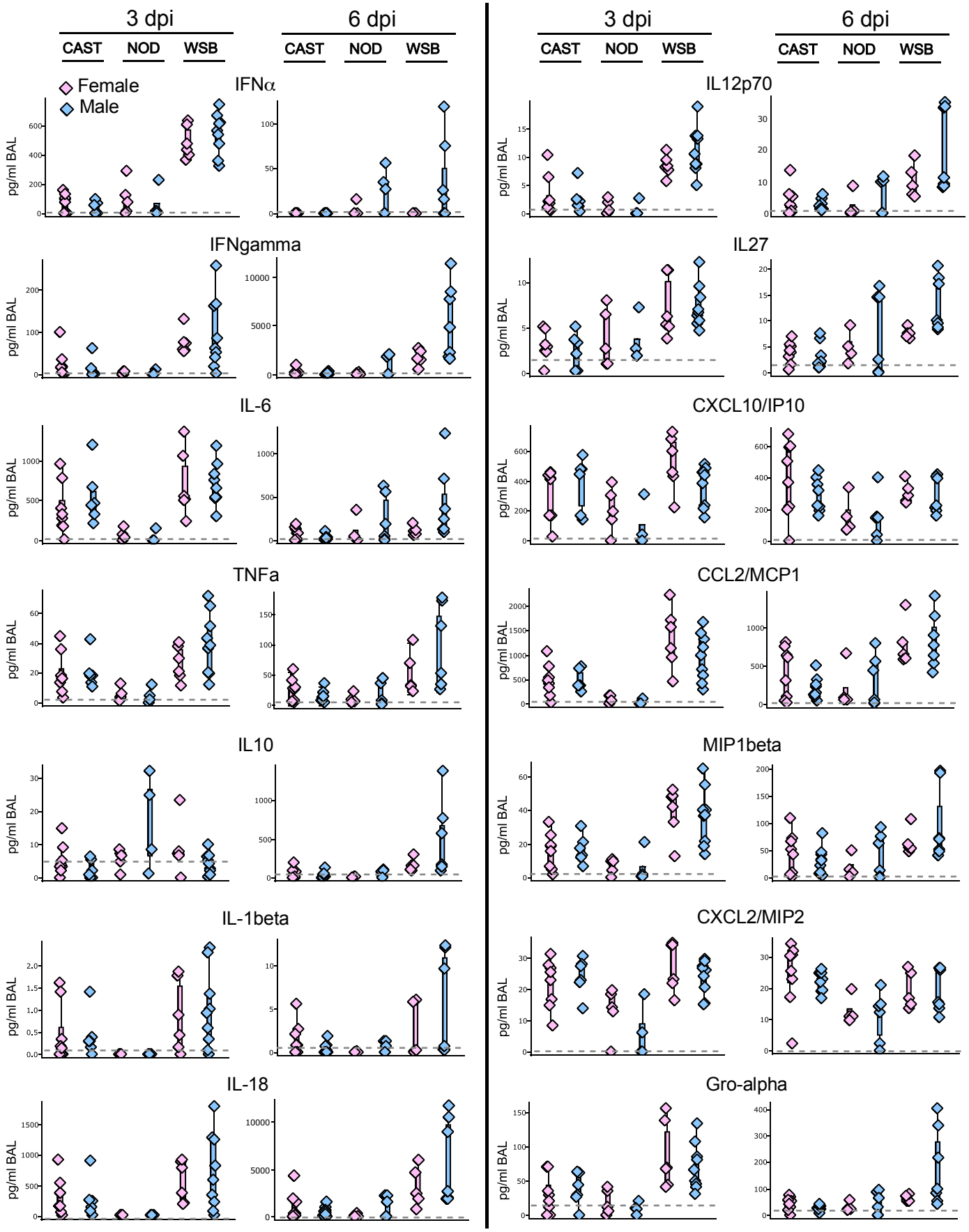
3 dpi
6 dpi
CAST
NOD
WSB
Female
Male
IFNα
IFNgamma
IL-6
TNFa
IL10
IL-1beta
IL-18
IL12p70
IL27
CXCL10/IP10
CCL2/MCP1
MIP1beta
CXCL2/MIP2
Gro-alpha
pg/ml BAL

Fig. S7